JOURNAL OF COMPUTATIONAL PHYSICS **127,** 27–51 (1996)
ARTICLE NO. 0156

A High-Resolution Hybrid Compact-ENO Scheme for Shock-Turbulence Interaction Problems

N. A. ADAMS* AND K. SHARIFF

Center for Turbulence Research, NASA Ames Research Center, MS 202 A-1, Moffett Field, California, 94035–1000

Received March 20, 1995; revised September 22, 1995

A class of upwind-biased finite-difference schemes with a compact stencil is proposed in general form, suitable for the time-accurate direct numerical simulation of fluid-convection problems. These schemes give uniformly high approximation order and allow for a spectral-like wave resolution while dissipating non-resolved wavenumbers. When coupled with an essentially non-oscillatory scheme near discontinuities, the compact schemes become shock-capturing and their resolution properties are preserved. The derivation of the compact schemes is discussed in detail. Their convergence and resolution properties as well as numerical stability are analyzed. Upwinding and coupling procedures are described. Application examples for typical non-linear wave interaction problems are given.

1. INTRODUCTION

For simple geometries a particularly attractive kind of discretization of the unsteady compressible Navier–Stokes equations are finite-difference schemes. In a method-of-lines approach the spatial discretization transforms the system of PDEs into a system of ODEs in terms of grid function values. The semi-discretized system is then integrated in time with a suitable integration method.

Standard finite difference methods obtain an approximation of a derivative of a grid function from a weighted average of the grid function on a subset of the grid (the stencil) which satisfies certain order conditions. This kind of semi-discretization we will call a *non-compact* finite-difference scheme. We note two features of non-compact finite-difference schemes which are troublesome. First, the stencil has to be at least one point wider than the approximation order. One then encounters the problem of finding suitable and stable boundary closures for high order schemes. Note that it has been shown [9] that boundary schemes must not be of order less than $(r-1)$ to mantain a global order r. Second, explicit finite difference schemes give a suboptimal representation of the dispersion relation with respect to the stencil width and free parameters. This problem is reflected in the fact that for wave-transport dominated problems a finer mesh spacing is required for an accurate representation of the dispersion relation than for an accurate approximation of the waveform itself at a time instant.

This study emphasizes the distinction between *order of approximation* and *resolution*. The first refers to a local Taylor expansion, and the local order of approximation of a spatial scheme is measured by the leading error term. The second refers to a Fourier expansion, and we measure the resolution of a scheme by the largest wavenumber ξ (normalized with the grid spacing h) of a single Fourier-mode $e^{-i\xi x}$ which can be accurately represented by the scheme. For general non-periodic solutions these criteria are not equivalent and the requirement of certain resolution properties imposes an additional restriction besides the order conditions. These additional restrictions may be satisfied by adjusting the coefficients of the finite difference scheme which are not fixed by the order conditions.

Additional free parameters can be obtained for a finite-difference scheme without increasing the stencil width (thus coping with the first problem of explicit schemes) by introducing a reconstruction from the above-mentioned weighted average. The scheme now has a non-trivial left-hand-side matrix since the reconstruction involves neighboring grid point derivative values. The additional free parameters may be used to achieve a high order with a narrow stencil. For that reason these implicit schemes are mostly called *compact* schemes. Members of this class have been proposed by Collatz [5], Hirsh [19], Kopal [21], Kreiss [23]. The free parameters may also be used to optimize resolution. A family of compact finite difference schemes with spectral-like resolution has been introduced by Lele [26]. Because of their similarity with schemes obtained from Padé-approximants we will refer to them as *Padé schemes*. Practical experience confirms that the family of schemes proposed in [26] have spectral-like resolution properties and a low absolute error level. They are used presently, e.g., for direct numerical simulations of transitional and turbulent shear flows [2, 8, 29, 30, 36].

* Present address: Swiss Federal Institute of Technology Zurich, Institute of Fluid Dynamics, ETH Zentrum, CH-8092 Zurich, Switzerland.

0021-9991/96 $18.00

In order to mimic spectral schemes, Padé schemes (except for boundary closures) have the inherent restriction of an assumed symmetry of their coefficients which makes them non-dissipative. As with spectral schemes the Padé schemes are sensitive to boundary condition formulation and aliasing errors. To cope with this sensitivity we drop in the present work the requirement of symmetric coefficients. By allowing for asymmetric coefficients the schemes can be upwind biased even with a centered stencil. The general formulation also trivially includes schemes on an upwind biased stencil by setting certain coefficients to zero, and it provides boundary closures as well. Through the upwind biasing a controlled amount of numerical dissipation is introduced implicitly at high wave numbers. The coefficients are found by solving the problem of optimal representation of the dispersion relation for a scalar advection equation under the constraint that the dissipation is bounded away from zero. A similar approach, with different emphasis, however, has been used in [13]. We also note that some particular forms of compact upwind schemes have been proposed earlier in [4, 6, 46].

A peculiar point is the construction of stable and order-consistent boundary closures for compact schemes. Once the interior scheme is Cauchy stable (i.e.,, the pure initial-value problem is stable) the stability of the global discrete differential operator is determined by the boundary closures. This is easy to see in light of a normal mode analysis (e.g., [44, Chap. 11]). Construction of stable high order boundary closures was the objective of [3], where the application of the so-called GKS theory [11] to semi-discretizations is also demonstrated. The analytic tractability of GKS theory for Padé schemes is based partially on the symmetry of their coefficients. Due to asymmetric coefficients and the bandwidth of the reconstruction operator (pentadiagonal for the schemes given in Section 2.4) an analysis by GKS theory is not tractable in general for the schemes presented here, even through the use of symbolic mathematics computer programs (at least with the authors' capacities). For the stability analysis of the general compact schemes we therefore resort to recent findings about the relation of stability of non-normal discrete derivative operators with their pseudo-spectra [33]. Although we do not obtain a closed expression which demonstrates stability independently of the number of grid points N, we find evidence for a sufficient condition for algebraic stability in a way similar to the von Neumann criterion (which is sufficient only for normal operators).

During the derivation of the compact schemes a real analytic solution is assumed. For weak solutions of conservative transport equations which may exhibit discontinuities, a special treatment is required. Two different approaches were investigated initially. The first is based on a TVB-limiter method [4]. Since reconstruction matrices of general compact schemes may be asymmetric and since we consider a finite domain problem this method required some modifications to be applicable for our schemes. Numerical tests (as in Section 6.1) demonstrated that this approach does not satisfactorily resolve discontinuities when applied to our schemes. Gibbs-like oscillations around shocks cannot be suppressed without a significant smearing of the shock. We do not discuss this approach further. In the second approach, following the basic idea of [18], we couple the non-conservative compact upwind scheme with a conservative shock-capturing scheme around discontinuities. For a different class of finite-difference schemes this procedure has a theoretical basis recently shown by [20]. Related approaches have been pursued by [15, 25]. Both are different from ours, however. The former differs from our approach in that a hybrid reconstruction from cell averages, switching from high-order to piecewise constant at discontinuities, is used to obtain numerical fluxes; in our case numerical fluxes from two different spatial discretization schemes are combined. The latter relies on a filtering step after the solution has been advanced by one (intermediate) time step using the underlying linear scheme. In the filtering step the numerical fluxes are corrected using an essentially non-oscillatory (ENO) scheme in critical regions. Our approach cannot be cast into the formalism of either of the above. Given a solution at time t_n a detection algorithm is used to identify cells which contain gradients too steep to be resolved and which thus require a special treatment. The flux derivative at the faces of such cells is then computed with a high order ENO scheme [41]. The linear compact scheme is then adapted to identically return the flux-derivatives computed by the ENO scheme in those regions and to give flux derivatives from the compact finite-difference scheme in the smooth regions. Note also that compact schemes are global schemes in general. An approach as in [25] would thus require a correction at (almost) each point of the domain.

In Section 2 we give the definition for the general form of compact finite-difference schemes. Approximation order and resolution are assessed in general terms and exemplified for two derived schemes. Numerical stability is discussed in Section 3. In Section 4 approximation order and stability are tested for a linear hyperbolic system. The objective of Section 5 is the coupling between compact finite-difference and ENO schemes. In Section 6 results for several test problems are given.

We finally note that a direct numerical simulation code using the proposed method has been developed [1] and is now being applied for the simulation of the interaction between turbulent boundary layers and shocks. This work is in progress and results will be reported elsewhere.

2. COMPACT FINITE DIFFERENCE SCHEMES

So far the most general form of compact finite-difference schemes has been given by [26]. In this section we drop

the requirement of symmetric/antisymmetric coefficients and arrive at a formulation which includes all linear finite-difference schemes (semi-discretizations only). We also give general formulas for numerical dispersion and dissipation and for the truncation error. Resolution and the approximation quality of a given scheme can be immediately assessed using these expressions. Two compact upwind schemes are derived, one with a higher dissipation at large wavenumbers (CUHD) than the other (CULD). Both have their special range of application. The former one may be used for direct numerical simulation (DNS) of turbulent flow, for instance, where aliasing errors resulting from non-resolved wavenumbers are suppressed and the scheme is also robust enough to be coupled with a nonlinear shock-capturing scheme. Note that the coupling region between a linear compact scheme and the non-linear ENO scheme is an inevitable source of spurious waves due to the non-constant stencil of the ENO scheme (see, e.g., [47]. The CULD scheme may be used for well-resolved DNS or large-eddy simulation without shocks, for instance, where some artificial dissipation at non-resolved wave numbers is required to inhibit odd–even decoupling observed in DNS with symmetric compact schemes [31].

2.1. Approximation Problem

Consider a function $f \in \mathscr{C}^{r+\sigma+1}$ on $x \in [0, L]$, $r, \sigma \in \mathbb{N}$, and an equidistant partition with spacing h of its domain by $\{x_j\} = \{x_0, ..., x_{N-1}\}$. We have the following approximation problem: given $\mathbf{f} = \{f(x_j)\}$, for $j = 0, ..., N-1$, seek an approximation $\tilde{f}^{\sigma}$ for $f^{(\sigma)} = d^{\sigma}f/dx^{\sigma}$ on $\{x_j\}$. Defining $\mathbf{M}_{\mathrm{L}}$ as the *left-hand* matrix and $\mathbf{M}_{\mathrm{R}}$ as the *right-hand* matrix of the scheme (for a non-compact finite-difference scheme $\mathbf{M}_{\mathrm{L}} = \mathbf{I}$) $\tilde{\mathbf{f}}^{\sigma}$ is obtained from

$$\mathbf{M}_{\mathrm{L}}\tilde{\mathbf{f}}^{\sigma} = \mathbf{M}_{\mathrm{R}}\mathbf{f}. \tag{1}$$

The entries α_μ of the ith row of $\mathbf{M}_{\mathrm{L}}$ and the entries a_ν/h^{σ} of the ith row of $\mathbf{M}_{\mathrm{R}}$ are obtained from a local ansatz at grid point x_i:

$$\sum_{\mu=-\mu_l}^{\mu_r} \alpha_\mu \tilde{f}_{i+\mu}^{(\sigma)} = \frac{1}{h^{\sigma}} \sum_{\nu=-\nu_l}^{\nu_r} a_\nu f_{i+\nu}. \tag{2}$$

We assume that $f(x)$ has a Taylor expansion up to order $\mathscr{O}(h^{r+\sigma})$ at each $x \in [0, L]$. The *local* approximation for $f^{(\sigma)}(x_i)$ is then determined from a Taylor expansion of $f(x)$ and $f^{(\sigma)}(x)$ about x_i. Assuming that neighboring values $\tilde{f}_{i+\mu}^{(\sigma)}$ are known for $\mu \in \{-\mu_l, ..., -1, 1, ..., \mu_r\}$, Eq. (2) then gives $\tilde{f}_i^{(\sigma)}$ with order $\mathscr{O}(h^{r+1})$. Note that (μ_l, μ_r) and (ν_l, ν_r) may differ, also (μ_l, μ_r) may be larger than (ν_l, ν_r), thus our formulation contains the cases of non-centered schemes where appropriate coefficients vanish.

2.2. Order Conditions

In this section we derive the equations to be satisfied by the coefficients α_μ and a_ν of the local schemes equation (2) in order to achieve an order of accuracy $(r+1)$. The local Taylor series expansions of $f^{(\sigma)}(x)$ and $f(x)$ up to order k about x_i are

$$f^{(\sigma)}(x_{i+\mu}) = \sum_{n=0}^{k} \frac{1}{n!} f^{(n+\sigma)}(x_i)(x_{i+\mu} - x_i)^n + R_k^{(\sigma)}(x_{i+\mu}) \tag{3}$$

and

$$f(x_{i+\nu}) = \sum_{n=0}^{l} \frac{1}{n!} f^{(n)}(x_i)(x_{i+\nu} - x_i)^n + R_l(x_{i+\nu}), \tag{4}$$

where $R_k^{(\sigma)}(x_{i+\mu})$ and $R_l(x_{i+\nu})$ are the corresponding Lagrangian remainder terms. Introducing these formulas into Eq. (2) and making use of the uniformity of the grid spacing one obtains

$$\begin{aligned} &\sum_{\mu=-\mu_l}^{\mu_r} \alpha_\mu \sum_{n=0}^{k} \frac{1}{n!} \mu^n f_i^{(n+\sigma)} h^n = \\ &\qquad \frac{1}{h^{\sigma}} \sum_{\nu=-\nu_l}^{\nu_r} a_\nu \sum_{n=0}^{l} \frac{1}{n!} \nu^n f_i^{(n)} h^n + \frac{1}{h^{\sigma}} \mathscr{O}(h^{\min(k+\sigma,l)+1}). \end{aligned} \tag{5}$$

If the required order of approximation is $r+1$ then the Taylor expansions must be carried out to $k \geq r$ and $l \geq r + \sigma$. After some manipulation Eq. (5) yields

$$\sum_{n=\sigma}^{r+\sigma} \sum_{\mu=-\mu_l}^{\mu_r} \frac{\alpha_\mu}{(n-\sigma)!} \mu^n f_i^{(n)} h^n \doteq \sum_{n=0}^{r+\sigma} \sum_{\nu=-\nu_l}^{\nu_r} \frac{a_\nu}{n!} \nu^n f_i^{(n)} h^n, \tag{6}$$

where "$\doteq$" denotes equality up to a term of order $\mathscr{O}(h^{r+1})$. By comparing coefficients of like powers of h in Eq. (6) and introducing

$$\delta(n) := \begin{cases} 1, & n \geq \sigma \\ 0, & n < \sigma, \end{cases}$$

one gets a system of linear equations to determine the coefficients α_μ and a_ν as

$$\delta(n) \frac{n!}{|n-\sigma|!} \sum_{\mu=-\mu_l}^{\mu_r} \mu^{n-\sigma} \alpha_\mu = \sum_{\nu=-\nu_l}^{\nu_r} \nu^n a_\nu \quad \text{for } n = 0, ..., r+\sigma. \tag{7}$$

This is a system with $(r + \sigma + 1)$ rows and $(\mu_r + \mu_l + 1 + \nu_r + \nu_l + 1)$ variables. One of the variables drops out

due to normalization, and satisfying the order conditions leaves $(\mu_r + \mu_l + \nu_r + \nu_l - m - \sigma)$ free parameters.

2.3. Truncation Error and Resolution Properties

We give a closed form estimate for the local truncation error $\mathscr{E}_c$ of Eq. (2) at x_i. Inserting the remainder terms according to Eqs. (3) and (4) into Eq. (2) gives, after some manipulation,

$$\mathscr{E}_c = \sum_{\nu=-\nu_l}^{\nu_r} (\nu h)^{r+1} \left[\frac{a_\nu \nu^\sigma}{(r+\sigma+1)!} - \frac{\alpha_\nu}{(r+1)!} \right] f^{(r+\sigma+1)}(x_c + \nu\theta h), \tag{8}$$

where $0 < \theta < 1$ and

$$\alpha_\nu := \begin{cases} \alpha_\mu, & \nu \in \{-\mu_l, \ldots, \mu_r\} \\ 0, & \text{otherwise.} \end{cases}$$

$\mathscr{E}_c$ can be estimated as

$$|\mathscr{E}_c| \le h^{r+1} \max_{\text{supp}} |f^{(r+\sigma+1)}(x)| \tilde{\mathscr{E}}_c, \tag{9}$$

where

$$\tilde{\mathscr{E}}_c = \left| \sum_{\nu=-\nu_l}^{\nu_r} \left(\frac{a_\nu \nu^\sigma}{(r+\sigma+1)!} - \frac{\alpha_\nu}{(r+1)!} \right) \nu^{r+1} \right| \tag{10}$$

and *supp* denotes the support of the stencil of the scheme.

As a model problem consider the linear advection equation on the half plane:

$$\frac{\partial u}{\partial t} + c \frac{\partial u}{\partial x} = 0, \quad t \ge 0, x \in (-\infty, +\infty). \tag{11}$$

A particular solution is given by

$$u(t, x) = e^{\mathbf{i}(\omega t - \xi x)} \tag{12}$$

where we call ω the frequency and ξ the wave number. Truncate the spatial domain to $x \in [0, 1]$, partitioned by $\{x_j\} = \{x_0, \ldots, x_{N-1}\}$ with uniform spacing h, and use the scheme of Eq. (1) to obtain

$$\mathbf{M}_\mathrm{L} \frac{d\mathbf{u}}{dt} + \frac{c}{h} \mathbf{M}_\mathrm{R} \mathbf{u} = 0, \tag{13}$$

where $\mathbf{u}$ is the N-component vector of gridpoint values. Assume that Eq. (13) has a solution of the form

$$u_i := e^{\mathbf{i}\tilde{\omega}t} v_i, \tag{14}$$

where $v_i = \mathrm{e}^{-\mathbf{i}\xi x_i}$. Then one obtains for row i of Eq. (13)

$$\tilde{\omega}(\xi) = \mathbf{i} \frac{c}{h} \frac{\sum_j M_r^{(ij)} v_j}{\sum_j M_l^{(ij)} v_j}. \tag{15}$$

This is the *approximate dispersion relation* : the numerical dissipation is $\mathrm{Im}(\tilde{\omega}^*(\xi))$ and the numerical dispersion is $\mathrm{Re}(\tilde{\omega}(\xi))$. The exact dispersion relation $\omega = c\xi$ implies the exact group velocity $c_\mathrm{g} = c$. Its approximate representation by the scheme is

$$\frac{d\tilde{\omega}(\xi)}{d\xi} = \mathbf{i} \frac{c}{h} \frac{d}{d\xi} \frac{\sum_j M_r^{(ij)} v_j}{\sum_j M_l^{(ij)} v_j}. \tag{16}$$

We note that the resolution properties are also affected by the time discretization method. For an explicit linear third-order Runge–Kutta time integration method, for instance, the full discretization $u^{(n+1)} = \Phi[u^{(n)}]$ of Eq. (11) is given by $\Phi = (1 + \mathbf{i}\tilde{\omega} - \frac{1}{2}\tilde{\omega}^2 - \mathbf{i}\frac{1}{6}\tilde{\omega}^3) u^{(n)}$. Herein we denote the time step index by n and assume the time step size for simplicity to be unity. For the full discretization the approximate frequency becomes

$$\tilde{\tilde{\omega}} = -\mathbf{i} \ln(1 + \mathbf{i}\tilde{\omega} - \tfrac{1}{2}\tilde{\omega}^2 - \tfrac{1}{6}\tilde{\omega}^3), \tag{17}$$

and the approximate group velocity is

$$\frac{d\tilde{\tilde{\omega}}}{d\xi} = \frac{1 + \mathbf{i}\tilde{\omega} - \frac{1}{2}\tilde{\omega}^2}{\cos\tilde{\tilde{\omega}} + \mathbf{i}\sin\tilde{\tilde{\omega}}} \frac{d\tilde{\omega}}{d\xi}. \tag{18}$$

Similar considerations apply for the advection equation in two dimensions,

$$\frac{\partial u}{\partial t} + \frac{\partial u}{\partial x} c\cos\theta + \frac{\partial u}{\partial y} c\sin\theta = 0, \tag{19}$$

which has a solution

$$u := e^{\mathbf{i}\omega t} e^{-\mathbf{i}\xi x \cos\theta} e^{-\mathbf{i}\zeta y \sin\theta}, \tag{20}$$

θ being the wave angle. Using the previous results we readily derive an approximation for the dispersion relation at (x_i, y_j) by scheme (1) as

$$\tilde{\omega}(\xi, \zeta; \theta) = \mathbf{i} \frac{c}{h} (\hat{A}_x(\xi\cos\theta) + \hat{A}_y(\zeta\sin\theta)), \tag{21}$$

where

$$\hat{A}_x = \frac{\sum_k M_r^{(ik)} v_{kj}}{\sum_k M_l^{(ik)} v_{kj}} \tag{22}$$

and

$$\hat{A}_y = \frac{\sum_l M_r^{(jl)} v_{il}}{\sum_l M_l^{(jl)} v_{il}}, \tag{23}$$

where $v_{ij} = e^{-\mathbf{i}\xi x_i \cos\theta} e^{-\mathbf{i}\zeta y_j \sin\theta}$. The group velocity is now a complex vector $\mathbf{c}_g \in \mathbb{C}^2$,

$$\mathbf{c}_g = -\mathbf{i} \begin{bmatrix} \dfrac{\partial \hat{A}_x}{\partial \xi} \\ \dfrac{\partial \hat{A}_y}{\partial \eta} \end{bmatrix}. \tag{24}$$

We note that the dispersion relation and group velocity in two dimensions can be obtained from the one-dimensional results by changing the wave number ξ to $\xi \cos\theta$ and $\eta \sin\theta$, respectively, and projecting the group velocity vector onto the normalized wave vector $\{\cos\theta, \sin\theta\}$. Since the resolution properties in more than one dimension can be represented by the one-dimensional results we restrict the following discussion to one dimension.

To diminish the local truncation error in certain regions (e.g., near large gradients) it is common practice to use a grid condensation or stretching. For a qualitative assessment of the effect of non-uniform grids we again consider the one-dimensional advection equation (11). Denote the mapping of the computational domain $\eta \in [0, 1]$ onto the physical domain $x \in [0, 1]$ as $\eta = \eta(x)$. From Eq. (15) we see that the approximate dispersion relation now becomes

$$\tilde{\omega}(\xi; x) = \mathbf{i} \frac{c}{h} \frac{d\eta}{dx} \frac{\sum_j M_R^{(ij)} v_j}{\sum_j M_L^{(ij)} v_j}. \tag{25}$$

In this equation $v_j = e^{-\mathbf{i}\xi x_j}$, where $\{x_j\}$ is not necessarily equispaced and $\tilde{\omega}(\xi; x)$ is a functional of the grid mapping $x(\eta)$.

For simplicity we assume that the grid distortion over the support of the scheme's stencil is not too strong, in other words, if we define $\chi(\eta) := x(\eta) - \eta$ we assume $\|\chi\| \ll 1$. The mapping $x(\eta)$ is thus restricted to functions with $\|x'(\eta)\| \simeq 1$ and $\|x''(\eta)\| \ll 1$. The Taylor expansion of the functional $e^{-\mathbf{i}\xi x}$ about $x(\eta) = \eta$ with respect to the function $x(\eta)$ can be written as

$$e^{-\mathbf{i}\xi x} = e^{-\mathbf{i}\xi\eta} + (-\mathbf{i}\xi) e^{-\mathbf{i}\xi\eta} \chi + \mathcal{O}(\chi\chi). \tag{26}$$

Inserting this relation, truncated after the first-order term, into Eq. (25) we obtain

$$\tilde{\omega}(\xi; x) \doteq \frac{\sum_\nu a_\nu e^{-\mathbf{i}\xi\eta_\nu}(1 - \mathbf{i}\xi\chi_\nu)}{\sum_\mu \alpha_\mu e^{-\mathbf{i}\xi\eta_\mu}(1 - \mathbf{i}\xi\chi_\mu)}. \tag{27}$$

After some manipulation we arrive at the approximation up to order $\mathcal{O}(\|\chi\|^2)$, where $\|\chi\|$ is assumed to be sufficiently small,

$$\tilde{\omega}(\xi; x) \doteq \frac{d\eta}{dx}(1 - \mathbf{i}\xi\varepsilon)\tilde{\omega}(\xi; \eta), \tag{28}$$

where

$$\varepsilon = \frac{\sum_\nu \sum_\mu a_\nu \alpha_\mu (\chi_\nu - \chi_\mu) e^{-i(\eta_\nu + \eta_\mu)\xi}}{\sum_\nu \sum_\mu a_\nu \alpha_\mu e^{-\mathbf{i}(\eta_\nu + \eta_\mu)\xi}}. \tag{29}$$

Since $\varepsilon \in \mathbb{C}$ in general, the grid mapping has a first-order perturbation by a term which corresponds to a rotation and stretching of $\tilde{\omega}(\xi; \eta)$ itself. The magnitude of the additional term depends on how close the mapped grid is to a uniform grid on the support of the stencil, i.e., the rapidity of the grid stretching.

If we neglect ε we have still to consider the effect of $d\eta/dx$:

(a) $d\eta/dx \in \mathbb{R}$ is known exactly; then the additional factor in Eq. (25) is just a stretching of the *modified wave number* $\tilde{\xi} = -\tilde{\omega}$; e.g., for a grid-point condensation $0 < dx/d\eta < 1$ it obviously means that the effective wave number $\tilde{\xi} dx/d\eta$ is reduced. Thus by decreasing the truncation error also the resolution is increased;

(b) $d\eta/dx \in \mathbb{R}$ is known approximately; the factor in Eq. (25) then becomes complex in general and the modified wavenumber suffers a combined rotation and stretching.

Note that even a non-dissipative scheme may become dissipative by using a grid mapping. As an illustration a little example is given in Appendix B.

For explicit upwind schemes it can be shown that for a split flux formulation they are equivalent to a symmetric scheme with an explicitly added dissipation term [17]. It might be worthwhile to point out that a similar relation holds for the compact upwind schemes. If we replace the flux F in a conservation equation,

$$\frac{\partial U}{\partial t} + \frac{\partial F}{\partial x} = 0,$$

e.g., by a Lax–Friedrichs flux $\hat{F}^{\pm} = \frac{1}{2}(F \pm \alpha U)$, where $\alpha = \max_j |\lambda_j|$ with λ_j being the eigenvalues of $\partial F/\partial U$, then

we arrive at the semi-discretization

$$\frac{\partial \mathbf{F}}{\partial x} \doteq \frac{1}{2}\left(\mathbf{M}_{\mathrm{L}}^{+-1} M_{\mathrm{R}}^{+} \otimes \hat{\mathbf{F}}^{+} + \mathbf{M}_{\mathrm{L}}^{--1}\mathbf{M}_{\mathrm{R}}^{-} \otimes \hat{\mathbf{F}}^{-}\right) + \frac{1}{2}\alpha\left(\mathbf{M}_{\mathrm{L}}^{+-1}\mathbf{M}_{\mathrm{R}}^{+} \otimes \mathbf{u} - \mathbf{M}_{\mathrm{L}}^{--1}\mathbf{M}_{\mathrm{R}}^{-} \otimes \mathbf{u}\right). \tag{30}$$

Herein we use "$\otimes$" as a symbol for the Kronecker product involving the $N \times N$ matrices $\mathbf{M}_{\mathrm{L,R}}^{\pm}$ and the $m \cdot N$ discrete flux vector $\hat{\mathbf{F}}^{\pm}$ (m is the number of flux components). A superscript "+" refers to a positively biased scheme while a superscript "−" refers to a negatively biased (for a definition see Section 2.5). $\mathbf{M}_{\mathrm{L}}^{-}$ and $\mathbf{M}_{\mathrm{R}}^{-}$ are obtained from $\mathbf{M}_{\mathrm{L}}^{+}$ and $\mathbf{M}_{\mathrm{R}}^{+}$ by multiplication with the positive and negative inverse unit matrix, respectively. The second term in Eq. (30) is a dissipation-free symmetric (except for the boundary closures) discretization of $\partial F/\partial x$ while the third term is a numerical dissipation of order $\mathcal{O}(h^{(r+1)})$. Both terms simplify and become equivalent to a symmetric compact scheme with an explicit dissipation term if $\mathbf{M}_{\mathrm{L}}^{+}$ is symmetric (i.e., $\mathbf{M}_{\mathrm{L}}^{+} = \mathbf{M}_{\mathrm{L}}^{-}$).

2.4. Optimal Resolution

In this section we derive a non-linear constrained optimization problem which gives a formal procedure for the selection of coefficients remaining free after satisfying the order conditions. A similar approach to derive optimal schemes for long-time integration has been used in [13].

Our scheme resolves an advection-type equation optimally if the error in the approximate complex dispersion relation is minimal. The error may be described by a suitable norm of the difference between the numerical and the exact dispersion relation. Considering the solution of an advection equation in spectral space an obvious choice is the L_2 norm giving the target functional as

$$\mathscr{E}_r = \alpha \int_0^{\Xi} [\tilde{\omega}_r(\xi) - \omega_r(\xi)]^2 \, d\xi + \beta \int_0^{\Xi} [\tilde{\omega}_i(\xi) - \omega_i(\xi)]^2 \, d\xi + \gamma \Pi(\xi^0). \tag{31}$$

Several parameters enter the definition of $\mathscr{E}_r$. The upper limit of integration in Eq. (31) is chosen as $\Xi \le \pi$. α is a weight for the dispersive error; β is a weight for the dissipative error. Π with the weight γ is a penalty function to be chosen. We require the scheme to satisfy two constraints:

(A) The LHS-matrix $\mathbf{M}_{\mathrm{L}}$ is required to be almost diagonally dominant (i.e., we enforce diagonal dominance at all rows except for finitely many at the boundaries):

$$\sum_{\substack{j=0 \\ j\neq 0}}^{N-1} |M_L^{(ij)}| \le \delta |M_L^{(ii)}|, \tag{32}$$

where $0 \le \delta < 1$. In this case the inverse of matrix $\mathbf{M}_{\mathrm{L}}$ is uniformly bounded (with respect to N).

(B) The scheme is required to satisfy a necessary stability criterion,

$$-\mathrm{Im}(\tilde{\omega}(\xi)) \ge 0 \tag{33}$$

(note that $-\mathrm{Im}(\tilde{\omega}(\xi))$ is obtained from Eq. (15)).

Condition (A) primarily allows one to solve Eq. (1) for $\tilde{\mathbf{f}}^{\sigma}$ safely without pivoting. Also, following the arguments in [4] (extended for the weaker case of an almost diagonally dominant matrix) condition (A) ensures the desirable property of a bounded reconstruction (i.e., solution of Eq. (1)) if the right-hand side is bounded. Condition (B) is without doubt reasonable and sorts out necessarily unstable schemes during optimization.

Locally optimal free coefficients which minimize $\mathscr{E}_r$ under the constraints (A) and (B) are obtained numerically. A standard sequential quadratic programming (SQP) method [37] is used. The selection of this algorithm was based on its ready availability (as IMSL routine NCONF) and on its superior performance and reliability compared to other approaches [37]. The algorithm is based on the iterative solution of the Lagrangian function associated with the constrained minimization problem by sequentially solving quadratic subproblems. These are obtained from a local quadratic approximation of the Lagrangian for each iteratively improved set of free coefficients. For details the reader is referred to [37, 43]. The optimization result strongly depends on the particular choice of parameters in Eq. (31) and is also sensitive to the initial guess.

We give two different schemes satisfying Eq. (7) each representing a local minimum of $\mathscr{E}_r$ with a locally (not necessarily globally) optimal set of free coefficients. Both schemes are consistently fifth order; i.e., they possess fourth-order boundary closures. The stencil width is 5 points, i.e., $\mu_l = \nu_l = \mu_r = \nu_r = 2$. The first scheme, called CUHD (compact upwind with high dissipation), is designed to be about as dissipative at non-resolved wave numbers as a non-compact upwind scheme (see [32]) while giving a much better representation of the dispersion relation. The second scheme, called CULD (compact upwind with low dissipation), is designed to be less dissipative (about one order of magnitude lower dissipation). We expect that this scheme is more sensitive to coupling with other schemes. In our case this concerns the shock capturing scheme at discontinuities. Schemes CUHD and CULD are obtained by minimizing slightly different target functionals equation (31) (see Table I) and by starting the optimization procedure from different initial guesses (see Table II). Target functional parameters and initial guesses are chosen so as to give a locally optimal solution which represents the previously mentioned basic properties of

TABLE I

Target Functional Parameters

	α		β		Ξ		γ		$\Pi(\xi_0)$	
Scheme	CUHD	CULD	CUHD	CULD	CUHD	CULD	CUHD	CULD	CUHD	CULD
ZS	2.4	2.8	0.5	0.6	2.3	2.3	0.04	0.4	$\omega_i(2)^2$	$\omega_i(2)^2$
LB1	1	1	0	0	2.1	2.1	0	0	—	—
LB2	1	1	1.96	0	2.3	2.3	0	0	—	—
RB2	1	1	0	0	2.3	2.3	0	0	—	—
RB1	1	1	0	0	2.3	2.3	0	0	—	—

Note. The following abbreviations are used: ZS stands for scheme at interior points, LB1 for scheme at the left boundary, RB1 for scheme at the right boundary, LB2 for scheme at the next-to-left boundary point, RB2 for scheme at the next-to-right boundary point.

the schemes (higher/lower dissipation). In practice the search for a locally optimal solution with the desired properties involved a significant amount of trial to find suitable target functional parameters and initial guesses. The coefficients of the schemes are given in Appendix A.

Figures 1 and 2 show the dispersion relation of the schemes CUHD and CULD, respectively. The contribution of the boundary schemes LB1,LB2 and RB1,RB2 to the overall resolution is small; they merely needed to be tuned to give a stable global discretization (Section 3). From the coefficients given in Appendix A it is evident that the interior scheme ZS of CULD is merely an asymmetric perturbation of a symmetric scheme which results in a low dissipation.

The truncation error estimate $\tilde{\tilde{c}}_c$ from Eq. (10) for the different schemes is given in Table III.

2.5. Upwinding

The schemes given in the previous subsection are upwind biased and thus only stable in the respective wind directions. They are only suitable for hyperbolic problems which allow for a diagonalization of the flux Jacobian. We denote an upwind scheme which is stable for $c > 0$ in Eq. (11) as *positively biased* and a scheme which is stable for $c < 0$ as *negatively biased*.

The upwinding procedure is straightforward. Consider a hyperbolic transport equation

$$\frac{\partial U}{\partial t} + \frac{\partial F}{\partial x} = 0, \tag{34}$$

where $F(U)$ is a homogeneous function of U and $\partial F/\partial U$ is hyperbolic. Then $\partial F/\partial U$ is similar to a diagonal matrix $\Lambda = S(\partial F/\partial U)S^{-1}$. First we calculate the positively and negatively biased approximate flux derivatives at x_i from

$$P_N^+(F)_i = (\mathbf{M}_{\mathrm{L}}^{+-1}\mathbf{M}_{\mathrm{R}}^{+} \otimes \mathbf{F})_i, \quad P_N^-(F)_i = (\mathbf{M}_{\mathrm{L}}^{--1}\mathbf{M}_{\mathrm{R}}^{-} \otimes \mathbf{F})_i. \tag{35}$$

These approximate flux derivatives are then projected on the local characteristics by left multiplication with the matrices of the left eigenvectors S_i^{-1} at x_i:

$$C_N^+(F)_i = S_i^{-1}P_N^+(F)_i,$$
$$C_N^-(F)_i = S_i^{-1}P_N^-(F)_i.$$

Defining the sign function as

$$\mathrm{sign}(\lambda) := \begin{cases} 1, & \text{if } \lambda > 0 \\ 0, & \text{if } \lambda = 0 \\ -1, & \text{if } \lambda < 0, \end{cases} \tag{36}$$

the approximation of the projected flux derivatives at x_i becomes finally after upwinding

$$C_N(F)_i = \tfrac{1}{2}[1 + \mathrm{sign}(\Lambda_i)]C_N^+(F)_i + \tfrac{1}{2}[1 - \mathrm{sign}(\Lambda_i)]C_N^-(f)_i. \tag{37}$$

TABLE II

Initial Guesses for Optimization

Scheme	Coefficient	CUHD	CULD
ZS	a_{-2}	0.3	0.1
	a_0	1.0	0.0
	a_2	0.01	−0.1
LB1	a_3	1.0	1.0
	a_4	1.5	1.5
LB2	a_2	1.0	0.0
	a_3	−1.	−0.2
RB1	a_{-4}	−1.	0.0
	a_{-3}	−1.	−1.0
RB2	a_{-3}	1.	1.
	a_{-2}	−1.	−1.

Note. Abbreviations are the same as Table I.

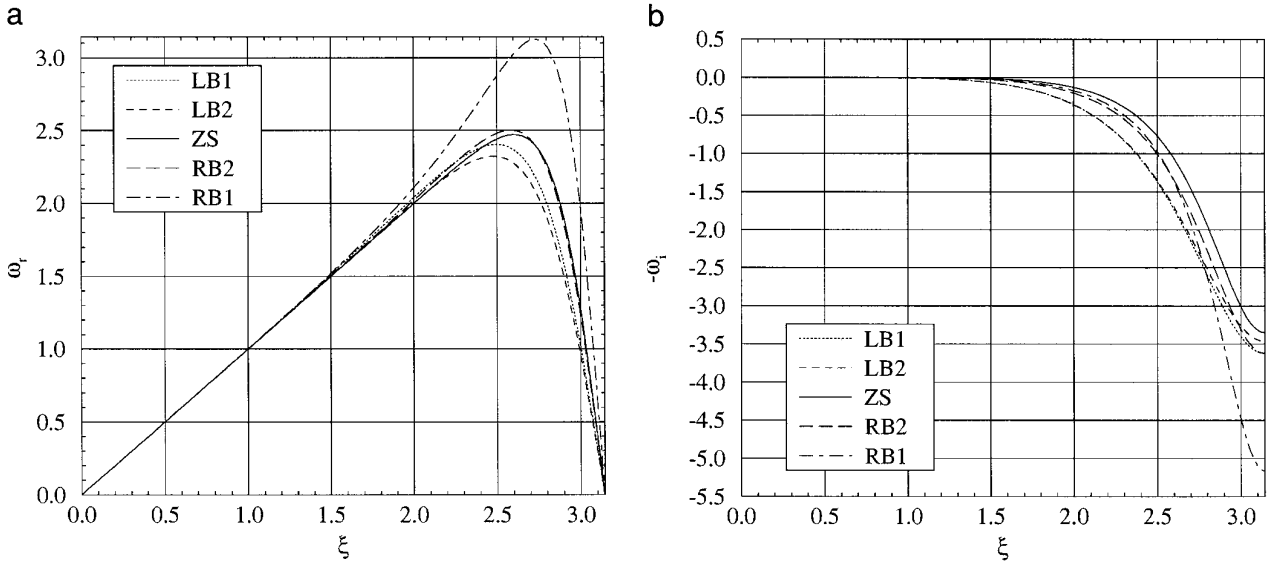

FIG. 1. Dispersion (a) and dissipation (b) for scheme CUHD. Abbreviations are the same as Table I.

By a projection back onto the basis of the computational space one gets

$$P_N(F)_i = S_i C_N(F)_i \tag{38}$$

for each x_i, $i = 0, ..., N - 1$. From Eq. (37) it can be seen that this upwind procedure yields an approximation of the flux derivatives which is for smooth fluxes continuous at least up to the approximation order of $P_N^+(F)$. It is a simple form of split fluxes [50].

3. NUMERICAL STABILITY

It is necessary to give evidence for the linear stability of the present scheme for a scalar advection equation, which serves as a model equation for the reduced hyperbolic part of the Navier–Stokes equations. Recent theoretical work shows that stable semi-discretizations lead to stable full discretizations when integrated with locally stable time integration schemes [24, 33]. The latter refers to the theory of pseudospectra and, roughly speaking, shows that a sufficient criterion for algebraic stability can be obtained

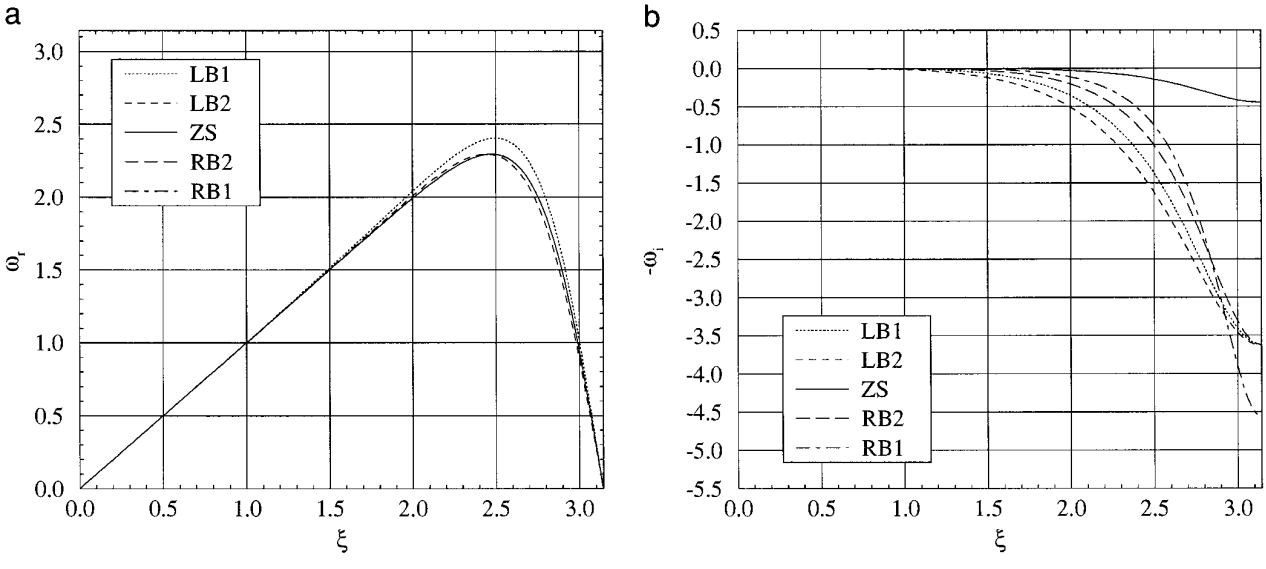

FIG. 2. Dispersion (a) and dissipation (b) for scheme CULD. Abbreviations are the same as Table I.

TABLE III

Truncation Error Estimate

Scheme	$\tilde{e}_c$ CUHD	$\tilde{e}_c$ CULD
ZS	0.200998	0.0334444
LB1	13.236	13.236
LB2	0.75466	3.35575
RB2	9.33802	9.33802
RB1	7.16414	6.51108

Note. Abbreviations are the same as Table I.

from a criterion similar to the von Neumann condition, however, in terms of pseudospectra.

Initially our intention was to design stable boundary closures for a given interior scheme by imposing GKS stability constraints (see, e.g., [44]) to the optimization procedure described in Section 2.4. This inverse problem of finding a family of stable boundary closures for a given interior scheme has been addressed in [3] without taking into account the resolution properties (thus leaving out the optimization part). For the upwind biased high order scheme this approach appears to be analytically intractable to us, even with extensive use of symbolic mathematics tools like *Mathematica* [49]. Instead we resort to the direct problem: given a certain semi-discretization, a sufficient criterion for stability is tested.

3.1. Stability via Pseudospectra

In the present context only linear stability is investigated; i.e., we consider an underlying hyperbolic system linearized about a mean. Even if non-linear stability is assured later by switching to a suitable non-linear scheme or using a flux-limiter near discontinuities the underlying scheme should be linearly stable to prevent the non-linear scheme or the limiter from becoming active in smooth regions or regions with resolvable gradients. A suitable scalar model equation is given by the homogeneous *advection equation*

$$\frac{\partial u}{\partial t} + \frac{\partial u}{\partial x} = 0, \quad 0 \le t < \infty, 0 \le x \le 1, \tag{39a}$$

with the boundary condition

$$u(0, t) = 0 \tag{39b}$$

and the initial condition

$$u(x, 0) = f(x). \tag{39c}$$

We consider a homogeneous equation only since an inhomogeneity, which is bounded on the strip, does not change the stability behavior of a discretization of Eq. (39a) (note that this is not necessarily true for non-linear problems and problems of a different type). Also it is sufficient to consider homogeneous boundary conditions since by a suitable change of variable boundary conditions can always be made homogeneous. We partition the interval [0, 1] into $\{x_j\}$ for $j = 0, ..., N-1$ with spacing h and denote the discretization of u by the N-component vector $\mathbf{v}(t) = \{v_j(t)\}$. With the right-hand side of the compact finite-difference operator denoted as $\mathbf{M}_\mathrm{R}$ and the left-hand side denoted as $\mathbf{M}_\mathrm{L}$ the semi-discretization of Eq. (39a) becomes

$$\mathbf{M}_\mathrm{L} \frac{d\mathbf{v}}{dt} = -\frac{1}{h} \mathbf{M}_\mathrm{R} \mathbf{v} \tag{40a}$$

with the boundary condition

$$v_0(t) = 0 \tag{40b}$$

and the initial condition

$$\mathbf{v}(0) = \{f(x_j)\}. \tag{40c}$$

Equation (40a) constitutes a linear system of ODE with constant coefficients with respect to the variable t. It is known that the general solution can be written as

$$\mathbf{v}(t) = \mathbf{C} e^{\mathbf{B}_h t} \mathbf{C}^{-1} \mathbf{v}(0), \tag{41}$$

where $\mathbf{B}_h$ is the Jordan normal form of $\mathbf{A}_h = -(1/h\ \mathbf{M}_\mathrm{L}^{-1}\ \mathbf{M}_\mathrm{R}$ with the regular transformation matrix $\mathbf{C}$. Stability of the semi-discretization requires

$$\|\mathbf{C} e^{\mathbf{B}_h t} \mathbf{C}^{-1}\| \le K(t) \quad \forall t \ge 0, \tag{42}$$

where $K(t)$ is bounded on each finite interval. We use $\|\cdot\| := \|\cdot\|_2$, the usual 2-norm. If $\mathbf{A}_h$ is a normal matrix then $\mathbf{B}_h$ is diagonal and $\mathbf{C}$ is unitary. Thus it is easy to see from Eq. (42) that for normal matrices a sufficient condition for Eq. (42) to be satisfied is that the real part of the spectrum of $\mathbf{A}_h$ be bounded. For non-periodic domains our schemes result generally in non-normal matrices $\mathbf{A}_h$ due to the boundary schemes. For a non-normal matrix $\mathbf{A}_h$, however, $\|\mathbf{C}\|$ is in general different from unity and becomes a function of h. Then a uniform estimate (42) is more difficult to obtain.

At this point we introduce the ε-pseudo-eigenspectrum of $\mathbf{A}_h$ according to [33]: *Given* $\varepsilon \ge 0$, *a number* $z \in \mathbb{C}$ *is an* ε*-pseudo-eigenvalue of* $\mathbf{A}_h$ *if* z *is an eigenvalue of* $\mathbf{A}_h + \mathbf{E}$ *for some complex matrix* $\mathbf{E}$ *with* $\|\mathbf{E}\| \le \varepsilon$ (other equivalent definitions are given in [33]).

With this definition we can restate the essential part of

Theorem 5.1 of [33]: *If for some constants K_0 and s the ε-pseudo-eigenvalues λ_ε of $\mathbf{A}_h$, where $\mathbf{A}_h$ has the dimension $N \leq \infty$, satisfy*

$$\mathrm{Re}(\lambda_\varepsilon) \leq s + K_0\varepsilon \quad \forall \varepsilon \geq 0 \tag{43}$$

then

$$\|e^{\mathbf{A}_h t}\| \leq eK_0 N e^{st} \quad \forall t \geq 0. \tag{44}$$

Besides the asymptotic stability of a semidiscretization (see end of this section), which roughly speaking ensures that a computation does not blow up while integrating forward in time, the correctness of the result is of main interest. For linear equations the Lax–Richtmyer equivalence theorem (see, e.g., [44]) ensures convergence by consistency and Lax-stability of the (semi-)discretization. Lax-stability of Eq. (40a) means that $\|e^{\mathbf{A}_h t}\|$ is bounded uniformly with respect to N on each finite interval $0 \leq t \leq T$. In our case, however, we arrive only at the weaker algebraic stability given by the preceding theorem. It can readily be shown that a generalized form of the equivalence theorem holds if the approximation error (and thus the consistency error) is of higher order with respect to N than the algebraic factor in Eq. (44). This has been pointed out in [7], we omit the proof here. Since we approximate the differential operators up to order $r^{+1} > 1$, giving accordingly a consistency error of same order, the generalized form of the equivalence theorem holds in our case given algebraic stability by Eq. (44), so that convergence is ensured. It remains to show that condition (43) holds for the semi-discretization. As mentioned in the introduction we do not give a strict proof but merely resort to an heuristic approach and investigate pseudospectra for some realizations for some $\varepsilon \geq 0$. A general behavior is then extrapolated without proof.

The ε-pseudo-eigenvalue problem for $\mathbf{A}_h$ is

$$(\mathbf{M}_\mathrm{L}\lambda_\varepsilon + \frac{1}{h}\mathbf{M}_\mathrm{R} - \mathbf{M}_\mathrm{L}\mathbf{E})\mathbf{w} = 0, \tag{45}$$

where $\mathbf{E}$ is a $N \times N$ matrix with $\|\mathbf{E}\| = \varepsilon$. We generate a realization for $\mathbf{E}$ by computing a random real number in (0, 1) for each component and then scale this matrix $\tilde{\mathbf{E}}$ by the square root of the spectral radius of $\tilde{\mathbf{E}}\tilde{\mathbf{E}}^*$, i.e., its 2-norm. Giving evidence for their stability is now a matter of a procedure almost as simple as testing the von Neumann criterion. Instead of computing the spectra of $\mathbf{A}_h$ we now have to solve the ε-eigenvalue problem equation (45). For practical purposes several simplifications are made. First, we solve Eq. (45) only for a finite number of $\mathbf{E}$, although the ε-pseudo-eigenspectra are the union of all eigenvalues of the characteristic equation (45) for all $\mathbf{E}$. Second, we draw our conclusions from only a finite number of different N. Figure 3 shows the pseudoeigenspectra for scheme CUHD and CULD for $N = 40$ and $N = 160$ and three different realizations of $\mathbf{E}$ for each ε. For clarity Fig. 4 shows the pseudospectra for CUHD near the imaginary axis at an enlarged scale. Figure 5 shows $|\mathrm{Re}(\lambda_\varepsilon)_{\max} - \mathrm{Re}(\lambda_0)_{\max}|$ for several N and three different realizations of $\mathbf{E}$. It is evident that each of the graphs is bounded above by a linear law $s + K_0\varepsilon$ for suitable constants s and K_0. This indicates the validity of condition (43) and thus the algebraic stability of the semidiscretization. For the final step we invoke Theorem 8.2 of [33] and arrive at a condition for algebraic stability of the full discretization for a locally stable one-step (e.g., Runge–Kutta) method. For time-integration methods of higher approximation order than 1 this again ensures convergence by the generalized equivalence theorem.

As mentioned before, Lax-stability is essential to ensure convergence of the discretization in terms of $h \to 0$ in a finite time interval. For long-time computations it also needs to be ensured that for a *fixed N* the computed solution does not become unbounded. This is the concept of *asymptotic stability*: *the semidiscretization* (40a) *is called asymptotically stable if for each eigenvalue λ of $\mathbf{A}_h$ (for fixed h) we have* $\mathrm{Re}(\lambda) < 0$, *or* $\mathrm{Re}(\lambda) = 0$ *and the algebraic multiplicity of λ is one.* We note from Fig. 3 that the condition for asymptotic stability is satisfied for CUHD and CULD.

3.2. Stability of the Cauchy Problem

Cauchy stability (besides being a necessary condition for stability of the initial boundary-value problem) is required for periodic boundary conditions or pure initial value problems. We drop the boundary conditions of Eq. (39a) and Eq. (40a) and restrict the domain to 2π-periodic functions. The semi-discretization is then given by the matrices $\mathbf{M}_\mathrm{L}$ and $\mathbf{M}_\mathrm{R}$ of the inner scheme which are now circulant. The generalized eigenvalue problem

$$(\mathbf{M}_\mathrm{L}\lambda + \frac{1}{h}\mathbf{M}_\mathrm{R})\mathbf{w} = 0 \tag{46}$$

now becomes

$$\lambda_j \sum_{\mu=-\mu_l}^{\mu_r} (M_\mathrm{L})_\mu^{(j,j+\mu)} \kappa_j^\mu = -\frac{1}{h} \sum_{\nu=-\nu_l}^{\nu_r} (M_\mathrm{R})_\nu^{(j,j+\nu)} \kappa_j^\nu,$$

where $\kappa_j = e^{\mathbf{i}j2\pi/N}$ are the N roots of unity. Consequently it is $\lambda = \mathbf{i}\tilde{\omega}(\xi)$ by Eq. (15) with $c = 1$, where we set $\xi = -2\pi j/N$. Since $\mathbf{M}_\mathrm{L}$ and $\mathbf{M}_\mathrm{R}$ are circulant $\mathbf{A}_h$ is circulant also. Thus $\mathbf{A}_h$ is normal and the von Neumann criterion is sufficient for stability. From Eq. (15) and Figs. 1b and

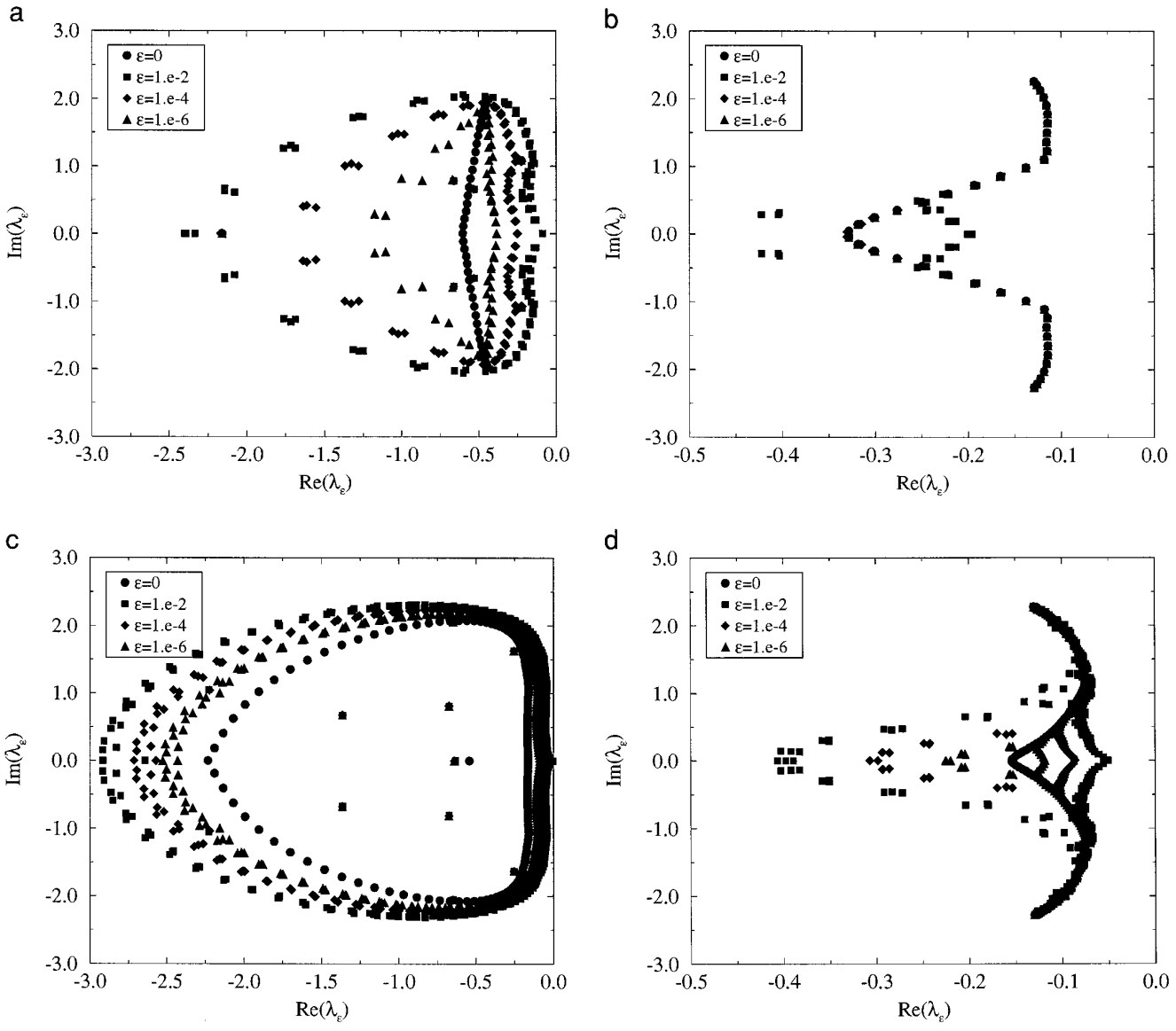

FIG. 3. ε-pseudo-eigenspectra for three different realizations of **E** for each ε; (a) CUHD, $N = 40$; (b) CULD, $N = 40$; (c) CUHD, $N = 160$; (d) CULD, $N = 160$.

2b it is evident that $\lambda < 0$ for $j = 1, ..., N - 1$ and $\lambda = 0$ for $j = N$ so that the von Neumann criterion is satisfied.

Expanding the real and imaginary part of λ for scheme CUHD in powers of the continuous wavenumber ξ about $\xi = 0$ one gets

$$\mathrm{Re}(\lambda) = -0.0142\xi^6 + 0.0849\xi^8 + \mathcal{O}(\xi^{12}) \qquad (47)$$

and

$$\mathrm{Im}(\lambda) = \xi - 0.0027\xi^7 + 0.0034\xi^9 + \mathcal{O}(\xi^{11}). \qquad (48)$$

Thus the approximation is dissipative of order $\alpha = 6$, given by the leading error term of the power expansion of $\mathrm{Re}(\lambda)$, and it is dispersive of order $\beta = 7$, given by the leading error term of the power expansion of $\mathrm{Im}(\lambda)$ (note that the first term represents the exact solution).

4. A NUMERICAL TEST

We test the convergence of the scheme for a time marching solution of an advection equation as used by Gustafsson [9]. We solve

$$\frac{\partial u}{\partial t} = \begin{bmatrix} 0 & -1 \\ -1 & 0 \end{bmatrix} \frac{\partial u}{\partial x}, \quad 0 \le x \le 1, \qquad (49a)$$

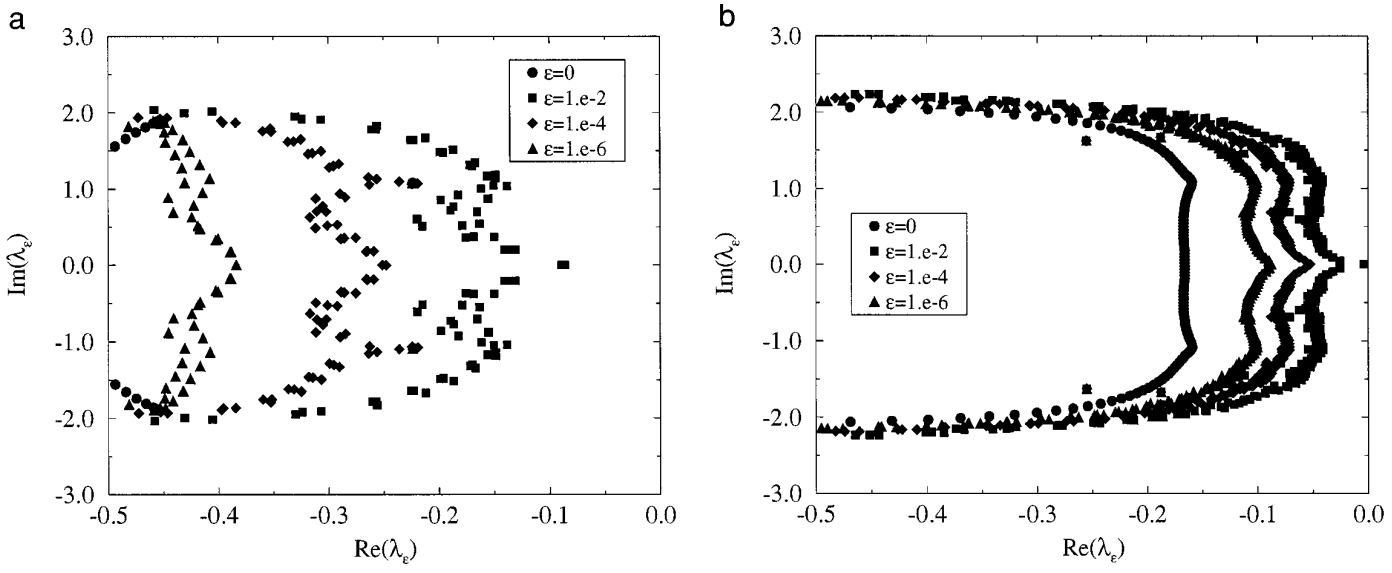

FIG. 4. Same as Figs. 3a and c, enlarged scale; (a) CUHD, $N = 40$; (b) CUHD, $N = 160$.

where $u = \{u^{\mathrm{I}}\, u^{\mathrm{II}}\}$, with the boundary condition

$$p(0) = \sin(2\pi t), \quad q(1) = \sin(2\pi t), \tag{49b}$$

where $p = u^{\mathrm{I}} + u^{\mathrm{II}}$ is the rightgoing and $q = u^{\mathrm{II}} - u^{\mathrm{I}}$ is the leftgoing Riemann variable. The initial condition is

$$u^{\mathrm{I}} = -\sin(2\pi x), \quad u^{\mathrm{II}} = 0. \tag{49c}$$

Thus the exact solution is

$$u^{\mathrm{I}} = -\cos(2\pi t)\sin(2\pi x), \quad u^{\mathrm{II}} = \sin(2\pi t)\cos(2\pi x). \tag{49d}$$

For the numerical approximation the interval [0, 1] is split into N equidistant subintervals. Using the Riemann variables p and q one obtains

$$\frac{\partial u}{\partial t} = \begin{bmatrix} -1/2 & -1/2 \\ -1/2 & 1/2 \end{bmatrix} \frac{\partial}{\partial x} \begin{bmatrix} p \\ q \end{bmatrix},$$

where the approximate derivatives of p and q are calculated

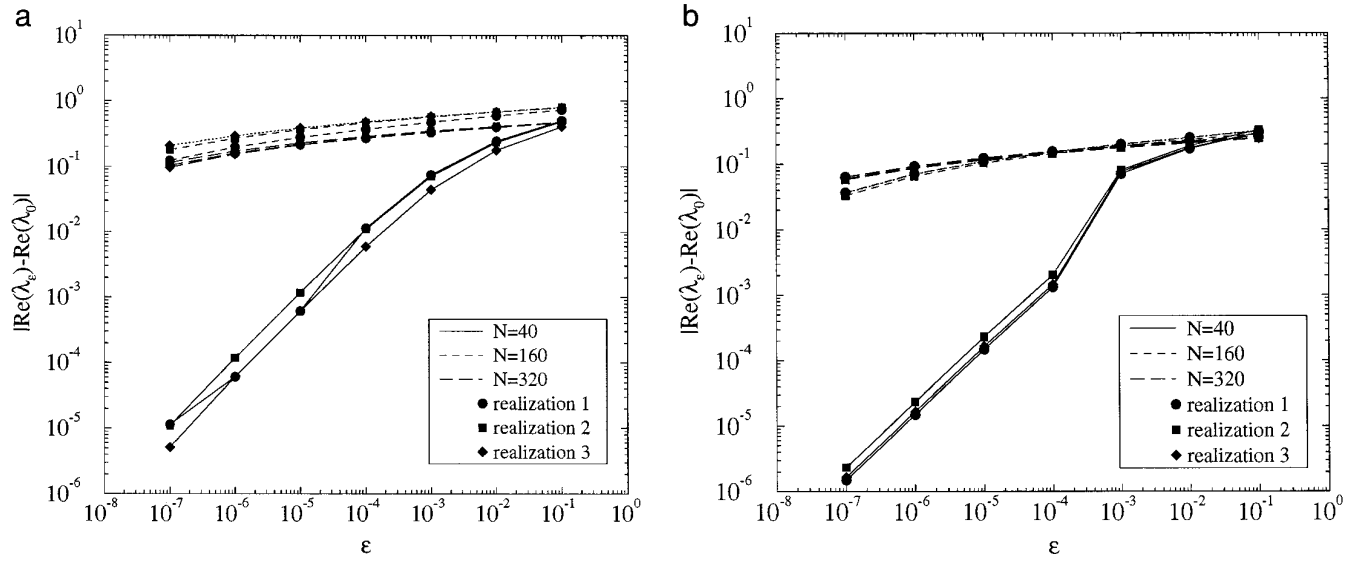

FIG. 5. Bound of $|\mathrm{Re}(\lambda_\varepsilon)|$; (a) CUHD; (b) CULD.

TABLE IV

L_2-Error at $t = 0.45$ and $t = 0.9$ for Schemes 455 and 346

	$t = 0.45$		$t = 0.9$	
N	CUHD	CULD	CUHD	CULD
25	6.94×10^{-5}	6.61×10^{-5}	1.01×10^{-4}	9.67×10^{-5}
50	2.16×10^{-6}	2.05×10^{-6}	3.12×10^{-6}	2.97×10^{-6}
100	6.74×10^{-8}	6.42×10^{-8}	9.71×10^{-8}	9.25×10^{-8}
200	2.11×10^{-9}	2.01×10^{-9}	3.03×10^{-9}	2.85×10^{-9}

by the corresponding upwind discretization. Time integration is performed with a sixth-order explicit Runge–Kutta method of the Butcher family [12]. This high order scheme has been chosen to suppress the effect of the time integration scheme on the approximation order while integrating with a fixed time step to mesh size ratio $\lambda = k/h$. Table IV shows the results for $\lambda = 0.5$. The error diminishes by a factor of about 2^5 for each twofold increase in the number of grid points.

5. SHOCK CAPTURING PROCEDURE

The compact schemes as derived in Section 2 are non-conservative in general and convergence to a weak solution of a scalar transport equation is not assured. In [20] it has been shown that a certain class of non-conservative finite-difference schemes gives solutions which converge to a weak solution if it is corrected towards a conservative scheme in a neighborhood of discontinuities. One assumption in the proof, which is only given for the Cauchy problem, is that the non-conservative scheme can be cast into incremental coefficients which satisfy a positivity condition (see also [14]). The compact schemes used here do not belong to this class. According to [4] a formulation by incremental coefficients is possible only in the means, i.e., for $\mathbf{M}_R\mathbf{u}$ of Eq. (13) but not for $\mathbf{M}_L^{-1}\mathbf{M}_R\mathbf{u}$. The numerical experiments of Section 6, however, give heuristic evidence that the main proposition of [20] also holds in our case if the compact schemes are coupled with a conservative ENO scheme around discontinuities. From a practical point of view this hybrid scheme has the advantage of circumventing well-known problems of an ENO scheme in smooth regions [35, 39], and also the computationally expensive non-linear apparatus of an ENO scheme is replaced by a simple linear one significantly increasing the overall efficiency of the scheme.

In a few words we outline the coupling procedure between the compact-FD and the ENO scheme. The details are to be found in the subsequent sections. First, a discontinuity detector algorithm (Section 5.3) marks cells to be treated by the ENO scheme. The marked regions are padded by a certain additional number of cells to allow the compact scheme on each side of the discontinuity to decouple and to allow the ENO scheme to fully expand its stencil. The fluxes at the centers of marked cells are calculated with an ENO procedure (section 5.1) and after reconstruction of flux derivatives at the cell faces, inserted into the appropriate places of the right-hand side of Eq. (13). This equation now can be understood as a scalar transport equation, where the spatial derivative is to be taken from a flux $F(U)$. The corresponding entries in the left-hand-side matrix are set to unity. The flux derivatives are then finally obtained by solving a pentadiagonal (in the case of schemes CUHD and CULD) linear equation system.

5.1. ENO Scheme

In this section we briefly summarize the ENO procedure used here. It follows [41] with differences only in the implementation.

We refer to Fig. 6. The numerical flux vector at the cell centers of marked cells $\hat{f}_{j+1/2}$ is calculated in the following manner. Define

$$\kappa(j,k) = \sum_{\nu=0}^{k} \prod_{\substack{\mu=j \\ p\neq j+\nu}}^{j+k} (1-\mu). \tag{50}$$

According to [41, 42] the numerical fluxes at the cell center $j + 1/2$ are then obtained by

$$\hat{f}_{j+1/2} = \sum_{m=0}^{r} \kappa(i-j,m)\overline{A}_{j+1/2}\,\Delta_{i,m}[\overline{A}_{j+1/2}^{-1} f], \tag{51}$$

where $\overline{A}_{j+1/2}$ stands for the Roe matrix at $j + 1/2$ [34]. With r we denote the order of the ENO scheme, which has accordingly $r + 1$ levels. For the definition of the operator $\Delta_{i,m}$ and the flux vector f we have to distinguish two cases depending on λ, the eigenvalues of $\partial F/\partial U$:

(a) For cell $j + 1/2$, if $\lambda_j < 0 < \lambda_{j+1}$ then a Roe-flux formulation may violate an entropy condition. In this case a local Lax–Friedrichs flux formulation is used and we define

$$f^{\pm} = \tfrac{1}{2}(F \pm \max_{j,j+1} |\Lambda| U) \tag{52}$$

and, recursively,

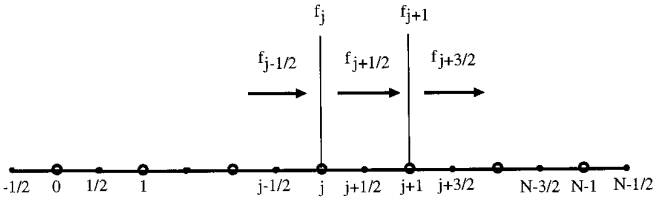

FIG. 6. Grid function and fluxes for ENO scheme.

$$\Delta^{\pm}_{i^{(m)},m} = \begin{cases} f^{\pm}[i^{(m-1)}, m],\ i^{(m)} = i^{(m-1)} - 1, \\ \qquad \text{if } |f^{\pm}[i^{(m-1)}, m]| \le |f^{\pm}[i^{(m-1)} + 1, m]| \\ f^{\pm}[i^{(m-1)+1}, m],\ i^{(m)} = i^{(m-1)}, \\ \qquad \text{if } |f^{\pm}[i^{(m-1)}, m]| > |f^{\pm}[i^{(m-1)} + 1, m]| \end{cases} \tag{53}$$

for $m = 0, ..., r$ and $i^{(0)} = j$ for Δ^+ and $i^{(0)} = j + 1$ for Δ^-. And finally it is

$$\Delta_{i^{(m)},m} = \Delta^{+}_{i^{(m)},m} + \Delta^{-}_{i^{(m)},m}. \tag{54}$$

(b) In case the former condition does not hold the less dissipative Roe flux formulation is used and we define

$$f = F \tag{55}$$

and recursively

$$\Delta_{i^{(m)},m} = \begin{cases} f[i^{(m-1)}, m],\ i^{(m)} = i^{(m-1)} - 1, \\ \qquad \text{if } |f[i^{(m-1)}, m]| \le |f[i^{(m-1)} + 1, m]| \\ f[i^{(m-1)+1}, m],\ i^{(m)} = i^{(m-1)}, \\ \qquad \text{if } |f[i^{(m-1)}, m]| > |f[i^{(m-1)} + 1, m]| \end{cases} \tag{56}$$

for $m = 0, ..., r$ and $i^{(0)} = j$, if $\overline{\lambda}_{j+1/2} \ge 0$ and $i^{(0)} = j + 1$ if $\overline{\lambda}_{j+1/2} < 0$.

After the projection step equation (51) the flux derivatives at the cell faces are reconstructed by

$$\hat{f}'_j = \frac{1}{h}(\hat{f}_{j+1/2} - \hat{f}_{j-1/2}). \tag{57}$$

5.2. Boundary Closures

Imposing stable and order preserving closures at the boundaries is an issue that is not so clearcut for ENO schemes. Harten *et al.* [16] suggest an extrapolation based on assumptions about the behavior of the three basic wave components of the Riemann problem at the boundary. This is unsatisfactory in particular at open or artificial boundaries.

In this study we use the following procedure. Instead of padding the computational domain with a border we restrict the stencil selection procedure from Eqs. (53) and (56) in the boundary regions by

$$i^{(m)} = \max(0, i^{(m-1)}) \quad \text{or} \quad i^{(m)} = \max(0, i^{(m)}) \tag{58}$$

for the left boundary and

$$i^{(m)} = \min(N - 1, i^{(m-1)}) \quad \text{or} \quad i^{(m)} = \max(N - 1, i^{(m)}) \tag{59}$$

for the right boundary, respectively. This in fact means that the stencil selection process is restricted to grid points belonging to the computational domain. The approximation order is unaffected by this restriction. Non-linear stability is no longer ensured at the boundary. Spurious waves generated at the boundaries can be expected to be extinguished by the ENO procedure within the domain before they reach a significant amplitude. To ensure non-linear stability, however, we have to introduce a TVB limiter at the boundaries which resembles a suggestion from [40]. The undivided differences calculated in Eqs. (53) and (56) are limited whenever j is closer to the boundary than $r + 1$ and if $m \ge 2$ by

$$\overline{\Delta}_{i^{(m)},m} := \text{sign}(1, \Delta_{i^{(m)},m}) \min(|\Delta_{i^{(m)},m}|, Kh^{m-2}), \tag{60}$$

where the constant K has to be chosen appropriately. If K is large enough and the solution is smooth, then this limiter should have no effect since $|\Delta_{i^{(m)},m}| < Kh^{m-2}$. In the examples presented below we choose $K = 10$.

5.3. Coupling with Compact Finite-Differences

Hybrid schemes require an algorithm which identifies regions where it is necessary to switch to the shock-capturing scheme. Presently we use a quite simple detection algorithm which has been suggested in [27]. More sophisticated detection algorithms could be employed but this one performs satisfactorily for the test problems shown below. It is important that the criterion is chosen in such a way that at least the cells containing a discontinuity are detected. If more than necessary cells are marked only the efficiency but not the accuracy of the scheme is affected.

Define

$$s_{j+1/2} := \frac{f_{j+1} - f_j}{h}. \tag{61}$$

If for cell $j + 1/2$ the following conditions are satisfied, the cell is treated with the ENO scheme:

(a) The modulus of the gradient times grid spacing is larger than a certain threshold

$$|s_{j+1/2}|h > \alpha_s. \tag{62}$$

(b) The gradient attains a local maximum

$$|s_{j-1/2}| < |s_{j+1/2}| \ge |s_{j+3/2}|. \tag{63}$$

Since ENO regions are padded by buffer regions, as mentioned below, there is no special treatment needed at the boundaries and the detection loop starts at cell 3/2 and ends at cell $N - 5/2$, where $j = 0, ..., N - 1$. Periodic boundaries are treated as such and the loop spans over all the grid points.

In the following we refer to Fig. 6. In case a gradient too steep to be resolved has been detected in cell $j + 1/2$, the flux vectors $f_{j-1/2}, f_{j+1/2}$, and $f_{j+3/2}$ are calculated with the ENO scheme equation (51) and the flux derivatives $\partial_x f_{j+1}$ and $\partial_x f_j$ at the faces of the marked cell are computed in the reconstruction step equation (57). In order to decouple pre- and post-discontinuity regions we need to pad identified transition cells on each side by at least $N_{sep} = 2$ points (which is the maximum of $\max(\nu_r, \mu_r)$ and $\max(\nu_l, \mu_l)$ for schemes CUHD and CULD). To allow the ENO scheme to fully expand to its linearly stable stencil without crossing the discontinuity we use generally $N_{sep} = (r + 1)/2 + 1$ if r is odd and $N_{sep} = r/2 + 1$ if r is even. Practical experience shows that a smaller N_{sep} may inhibit the ENO apparatus from stabilizing the solution.

The coupling procedure is in summary the following:

(1) Identify the critical cells, mark them, and N_{sep} additional buffer cells on each side to be treated by the ENO scheme. This gives an identification vector for $j = 0, ..., N - 1$,

$$\Upsilon(j) = \begin{cases} \text{true}, & \text{if marked} \\ \text{false}, & \text{else} \end{cases} \tag{64}$$

(the reader familiar with FORTRAN 90 may note that Υ functions as a mask in the procedure).

(2) Compute fluxes at the cell centers of marked cells $\hat{f}_{j+1/2}$ and reconstruct flux derivatives at the corresponding cell faces $\partial_x \hat{f}_j$.

(3) Compute the flux derivatives for each $j = 0, ..., N - 1$:

(3.1) calculate $\mathbf{M}_R^{\pm} \otimes \mathbf{F}$;

(3.2) for each $j = 0, ..., N - 1$ replace the entry in $\mathbf{M}_R^{\pm} \otimes \mathbf{F}$ by $\hat{f}_j$ if $\Upsilon(j)$ is true;

(3.3) for each $j = 0, ..., N - 1$ replace the rows i in $\mathbf{M}_L^{\pm}$ by δ_{ij} if $\Upsilon(j)$ is true;

(3.4) solve the so obtained modified equation

$$\tilde{\mathbf{M}}_L^{\pm} \otimes \mathbf{F}' = \tilde{\mathbf{M}}_R^{\pm} \otimes \mathbf{F}$$

for $\mathbf{F}'$;

(3.5) perform the upwinding according to Section 2.5.

(4) Project the solution forward in time.

For systems of equations the procedure is performed subsequently for each of the flux-vector components.

6. NUMERICAL EXAMPLES

In this section we present some 1D and 2D IVP and IBVP which can be considered as model problems for typical phenomena in the computation of flows governed by the Euler equations.

6.1. Inviscid Burgers' Equation

The simplest model for non-linear wave interactions analogous to the Euler equations is given by the inviscid Burgers equation. A more elaborate discussion of this model problem can be found in [22], for example, which deals with fundamentals and [10] which concerns numerical approximations.

6.1.1. *Problem Formulation*

We solve

$$\frac{\partial u}{\partial t} + \frac{\partial}{\partial x}\left(\frac{u^2}{2}\right) = 0, \quad x \in [-1, 1], t \geq 0, \tag{65}$$

with $u(x)$ being 2-periodic in x. The initial condition is given by

$$u(0, x) = \alpha + \beta \sin \pi(\xi + \gamma), \tag{66}$$

where α, β, γ are parameters and $\xi := x - \alpha t + \gamma$.

The exact solution for this problem is obtained by the following procedure. Define

$$\mathrm{Z} := \sin \pi(\xi - \mathrm{Z}\tau), \tag{67}$$

where $\xi := x - \alpha t + \gamma$ and $\tau := \beta t$. Then

$$\frac{\partial \mathrm{Z}}{\partial \xi} = \frac{\pi \cos \pi(\xi - \mathrm{Z}\tau)}{1 + \pi\tau \cos \pi(\xi - \mathrm{Z}\tau)}$$

and

$$\frac{\partial \mathrm{Z}}{\partial \tau} = \frac{-\mathrm{Z}\pi \cos \pi(\xi - \mathrm{Z}\tau)}{1 + \pi\tau \cos \pi(\xi - \mathrm{Z}\tau)}$$

which, when put into Eq. (65) using the ansatz $u(t, x) := \alpha + \beta \mathrm{Z}(\tau, \xi)$, give a transcendental equation to be solved at each (τ, ξ),

$$\mathrm{Z}(\tau, \xi) = \sin \pi(\xi - \mathrm{Z}(\tau, \xi)\tau). \tag{68}$$

It follows from this equation that Z is anti-symmetric in ξ so that one obtains the solution for $\xi \in [-1, 0)$ by using the solution for $\xi \in [0, 1]$. For $\xi \notin [-1, 1]$ the solution is obtained from the solution for a $\tilde{\xi} = \mathrm{mod}(\xi + 1, 2) - 1$. The position of the shock evolving from nonlinear wave interaction can be determined from the observation that the denominator of $\partial Z/\partial \xi$ approaches 0 in this case. Then it is readily derived that at $t = (\beta\pi)^{-1}$,

$$x_{\mathrm{shock}} = 1 + \frac{\alpha}{\beta\pi} - \frac{\gamma}{\pi}. \tag{69}$$

6.1.2. *Numerical Solution*

We solve Eq. (65) with the parameters $\alpha = 0.3, \beta = 0.7$, and $\gamma = \pi$. The methods employed resemble those which will be of interest for later large-scale simulations :

(A) E5TVDR3. Using a Roe–LLF–ENO scheme [41] of fifth-order in space and a third-order TVD Runge–Kutta scheme in time [38].

(B) CUHDE5R3. Using the upwinded compact scheme CUHD in space, switching to fifth-order Roe–LLF–ENO at discontinuities, and a third-order Runge–Kutta scheme in time (Williamson's case 7 [48]).

(C) CULDE5R3. Using the upwinded compact scheme CULD in space, switching to fifth-order Roe–LLF–ENO at discontinuities, and a third-order Runge–Kutta scheme in time (Williamson's case 7 [48]).

We use $N_{\mathrm{sep}} = 4$ and set the shock detector parameter to $\alpha_s = 0.1$. The grid spacing is equidistant and CFL = 0.5, where the time step is estimated by $\tau = \mathrm{CFL}/\max(u/h)$.

For discontinuous solutions the error norms are calculated in the smooth regions, excluding $x_{\mathrm{shock}} - 0.1 < x < x_{\mathrm{shock}} + 0.1$.

At $t = 0.3$ the solution is still continuous, although wave-steepening has strongly deformed the initial sinusoidal profile, (Fig. 7). At $t = 2/\pi$ a shock is present and has already been convected some distance through the domain, so that we also can check for the correct convection velocity. From Fig. 7 we see that the hybrid scheme is able to capture the shock with no more than three points and that the discontinuity has been convected correctly.

In Fig. 8 we compare the convergence of the different schemes for the smooth solution at $t = 0.3$ and at $t = 2/\pi$. We note that for the smooth solution the ENO-scheme suffers from the well-known order-degeneracy phenomenon [35, 39] (note that we did not employ a center-biasing suggested as a remedy in [39]). The compact schemes converge at $1/N^5$ for low N and $1/N^3$ at large N, the latter of which is the expected asymptotic convergence rate, due to the fact that we used a third-order time integration scheme, together with a fifth-order spatial discretization and a constant CFL number.

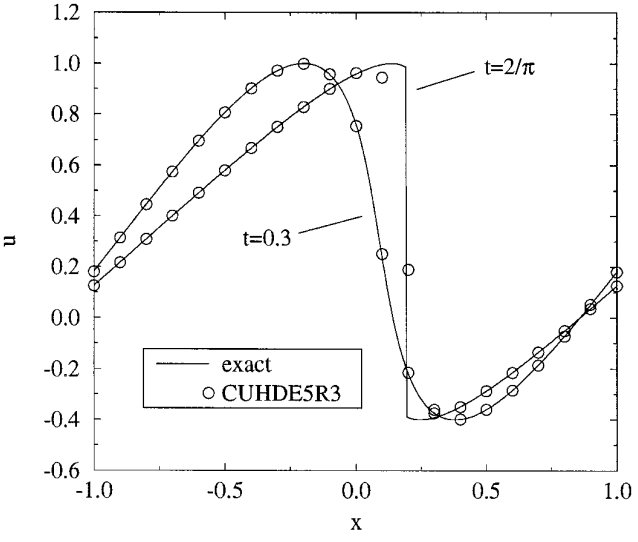

FIG. 7. Solution for Burgers' equation, $N = 20$.

For the discontinuous solution we observe that the order-degeneracy problem of the ENO-scheme disappears. The hybrid scheme CUHDE5R3 converges at a rate between $1/N^5$ and $1/N^3$ while the less dissipative scheme CULDE5R3 suffers from spurious waves generated at the interface between ENO and Padé schemes as will be seen later from the local error distributions. Nevertheless scheme CULDE5R3 remains stable, converges at about a rate $1/N^3$, and gives the correct non-linear wave transport.

We also note that scheme B (for $N = 80$) was 6.4 times faster than scheme A. This relation becomes even more favorable for the hybrid schemes with increasing N. For this run the hybrid scheme treated over the 51 time steps an average of 4.98% points by the ENO procedure. We refer a set of contiguous points treated by the ENO procedure as an ENO cluster. In the present calculation there were an average of 0.45 clusters.

To demonstrate that the hybrid scheme maintains the theoretical order of the spatial scheme, we give the error norms at $t = 2/\pi$ in Fig. 9 for scheme CUHDE5R6, where we exchanged the third-order Runge–Kutta scheme with the sixth-order scheme from Section 4.

Finally, Fig. 10 shows the distributions of the local error at $t = 2/\pi$ with $N = 80$. We note that the hybrid schemes capture the shock with the same accuracy as the pure ENO scheme. For the hybrid scheme CULDE5R3, we see that some spurious waves are generated at the interface between the compact and the ENO scheme and penetrate into the smooth regions.

6.2. Shock Wave Interacting with Fluctuations, 1D

In this section we briefly investigate a simple 1D model problem for shock–turbulence interaction as suggested in

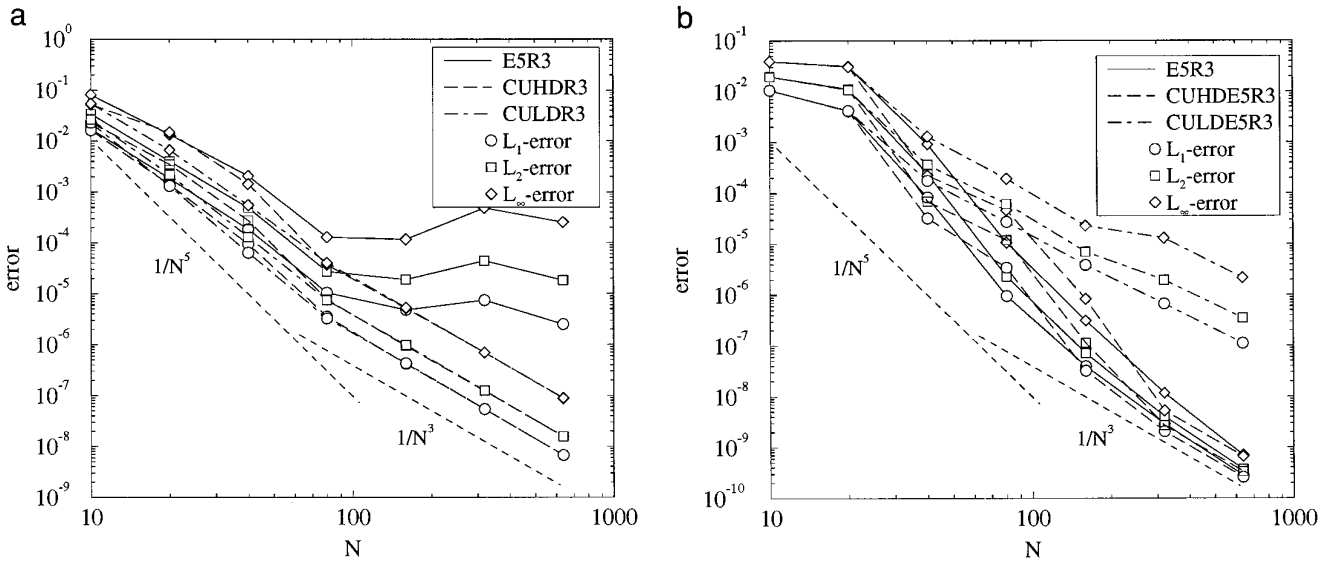

FIG. 8. Error norms; (a) at $t = 0.3$; (b) at $t = 2/\pi$.

[41]. The 1D Euler equations constitute a Riemann problem which is solved with method CUHDE5R3. In the present case a $M = 3$ shock is moving into a density (or entropy) fluctuation field. Results for this problem obtained with a pure ENO scheme have been presented in [41].

6.2.1. *Problem Formulation*

We write the 1D Euler equations as

$$\frac{\partial \mathbf{u}}{\partial t} + \frac{\partial \mathbf{F}}{\partial x} = 0$$

on the half-strip $(t, x) \in [0, \infty) \times [-5, 5]$. We denote the vector of dependent variables by $\mathbf{u} := \{\rho, \rho u, E\}$, where ρ is the density, u is the velocity, and $E = p/(\kappa - 1) + \rho u^2/2$ is the total energy (p being the pressure). The flux vector is $\mathbf{F} := \{\rho u, \rho u^2 + p, u(E + p)\}$. We impose an initial condition in accordance with [41] as

$$\mathbf{u}(0, x) = \begin{bmatrix} 3.857143 \\ 2.629369\, u_1(0, x) \\ \dfrac{31/3}{\kappa - 1} + \dfrac{1}{2}\dfrac{u_2(0, x)^2}{u_1(0, x)} \end{bmatrix} \quad \text{if } x < -4$$

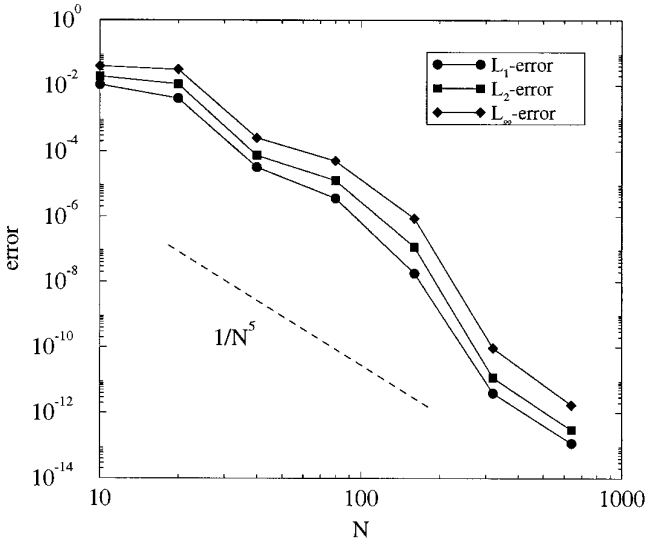

FIG. 9. Error norms for Burgers' equation at $t = 2/\pi$.

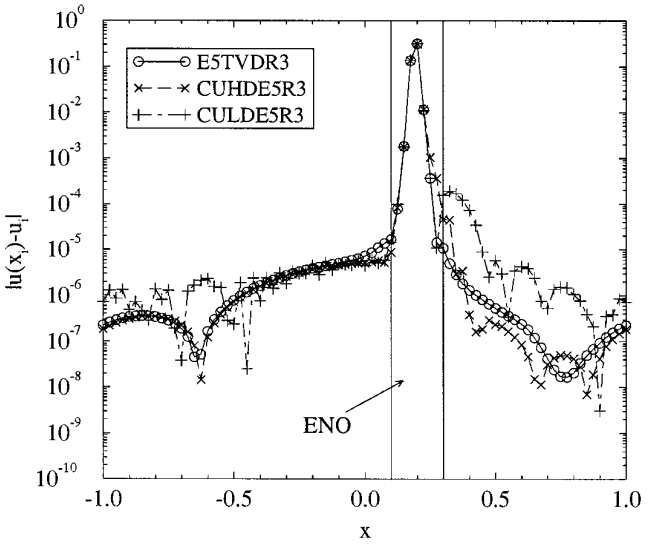

FIG. 10. Local error at $t = 2/\pi$, $N = 80$.

$$\mathbf{u}(0,x)=\begin{bmatrix}1+0.2\sin 5x\\ 0\\ 1/(\kappa-1)\end{bmatrix}\quad \text{if } x\geq -4,$$

where κ has been set to 1.4. Boundary conditions imposed to make the problem well posed are

$$u_1(t,-5)=3.857143$$
$$u_2(t,-5)=2.629369\,u_1(t,0)$$
$$u_3(t,-5)=\frac{31/3}{\kappa-1}+\frac{1}{2}\frac{u_2(t,0)^2}{u_1(t,0)}$$

at the left boundary (supersonic inflow) and

$$u_2(t,5)=0$$

and at the right boundary (one incoming characteristic). Neglecting the effect of the perturbation, the shock would move with speed

$$\overline{u}=\left[\frac{p_2-p_1}{\rho_2-\rho_1}\frac{\rho_2}{\rho_1}\right]^{1/2}$$

(indices "1" and "2" denote the pre- and post-shock conditions, respectively) which from the initial data can be estimated as $\overline{u}=3.55$. At $t=1.8$ (the time at which we show the numerical results below) the shock should have moved from $x=-4$ to $x=2.39$ (the reader may note that this coincides perfectly with the results).

6.2.2. *Numerical Solution*

The detector parameter is chosen as $\alpha_s=1.2$ and $N_{\text{sep}}=4$. In all cases CFL = 0.5 is used and the time step is estimated by

$$\tau=\text{CFL}\left[\max_{\mathscr{D}}\left(\frac{u}{h},\frac{u-c_s}{h},\frac{u+c_s}{h}\right)\right]^{-1}.$$

We present the obtained results at $t=1.8$ for an increasingly fine mesh in Figs. 11–13. The entropy difference $\Delta s/c_p$ uses the undisturbed pre-shock state as reference. As reference solution a calculation made with $N=1600$ is taken. The run for $N=200$ with the hybrid scheme was by about a factor of 3 faster than the pure ENO scheme of the same spatial/temporal order. For this case 14.2% of all grid points were treated on the average with ENO, and the average number of ENO clusters was 1.6. For $N=400$ these values were 10.6% and 1.4, respectively, showing that efficiency increases with N.

Similar results, but with small spurious post-shock oscillations in the uniform velocity behind the shock (where the perturbation has not yet propagated), are obtained with scheme CULDE5R3. The results compare well with a pure ENO scheme of the same order.

6.3. Shock Wave Interacting with Fluctuations, 2D

Finally we investigate a simple 2D model problem for shock–turbulence interaction as suggested in [41]. The 2D Euler equations constitute a Riemann problem which is solved with method CUHDE5R3.

6.3.1. *Problem Formulation*

We write the 2D Euler equations as

$$\frac{\partial\mathbf{q}}{\partial t}+\frac{\partial\mathbf{F}}{\partial x}+\frac{\partial\mathbf{G}}{\partial y}=0$$

on the domain $(t;x,y)\in[0,\infty)\times[-1.5,1.5]\times[-1,1]$. We denote the vector of dependent variables by $\mathbf{q}:=\{\rho,\rho u,\rho v,E\}$, where $E:=p/(\kappa-1)+\rho(u^2+v^2)/2$. The flux vectors are $\mathbf{F}:=\{\rho u,\rho u^2,+p,\rho uv,u(E+p)\}$ and $\mathbf{G}:=\{\rho u,\rho uv,\rho v^2+p,v(E+p)\}$. The initial conditions constitute a $M_s=8$ shock moving into an oblique divergence free vorticity fluctuation field. From shock relations (e.g., Thompson [45]) the shock propagation velocity is

$$\overline{u}=M_s c_{s1},$$

where c_s is the speed of sound (we denote with "1" the pre-shock state and with "2" the post-shock state). The initial pre-shock state ($x\geq 1$) is

$$u(x,y):=-c_{s1}\sin\theta\cos(xk\cos\theta+yk\sin\theta)$$
$$v(x,y):=c_{s1}\cos\theta\cos(xk\cos\theta+yk\sin\theta)$$
$$\rho(x,y):=1$$
$$p(x,y):=1$$

with the parameters $\theta=\pi/6$, $k=2\pi$, while the corresponding initial post-shock state ($x<1$) is

$$u(x,y):=\frac{2+(\kappa-1)M_s^2}{(\kappa-1)M_s^2}\overline{u}$$
$$v(x,y):=0$$
$$\rho(x,y):=\frac{(\kappa+1)M_s^2}{2+(\kappa-1)M_s^2}\rho_1$$
$$p(x,y):=p_2:=\left(1+\frac{2\kappa}{\kappa+1}(M_s^2-1)\right).$$

Thus $c_{s1}=\sqrt{\kappa}$, where κ has been set to 1.4.

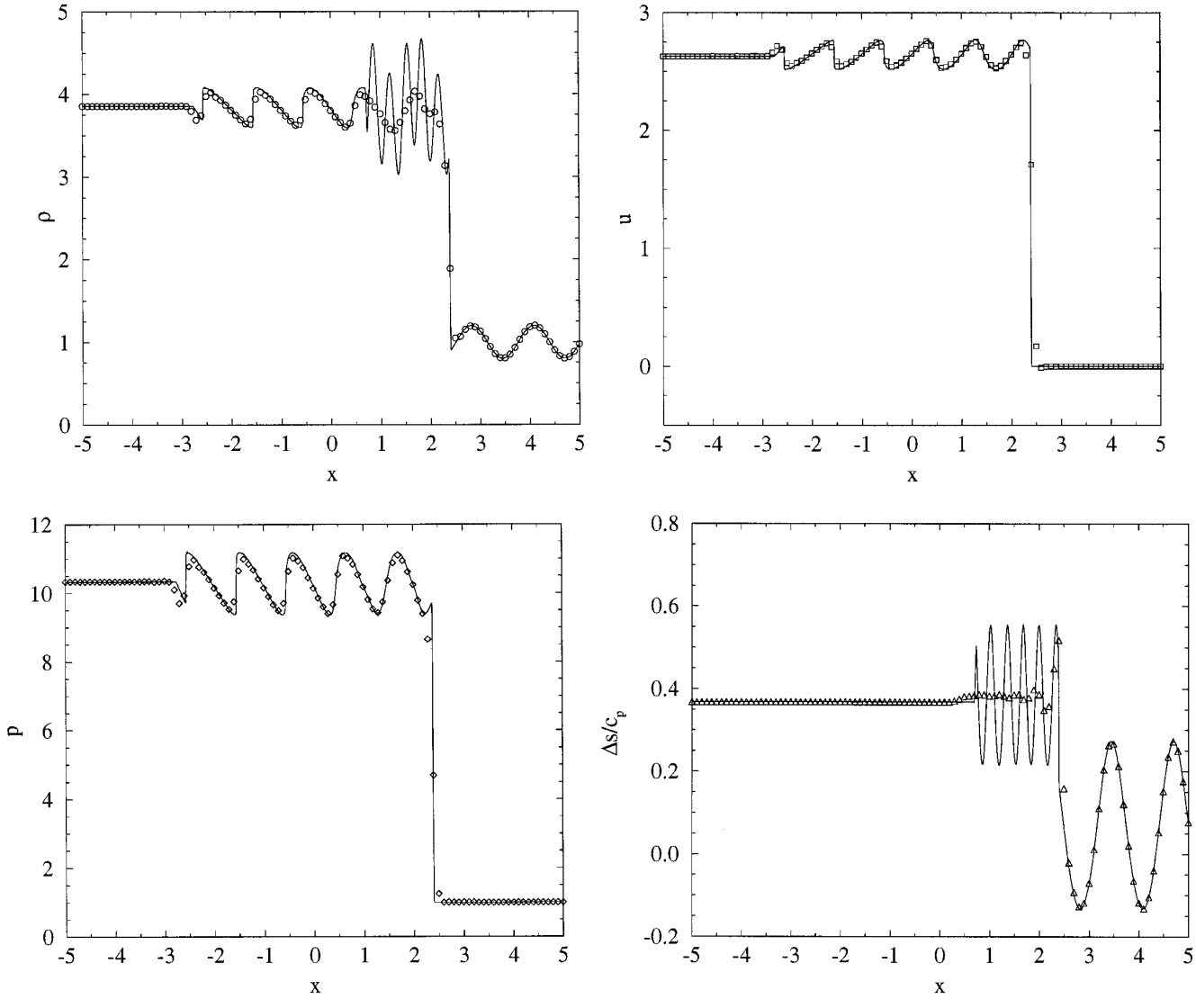

FIG. 11. Shock wave interacting with fluctuations at $t = 1.8$, scheme CUHDE5R3, $N = 100$. The solid line represents the solution computed with $N = 1600$.

Boundary conditions imposed to make the problem well posed are:

$$\begin{aligned} q_1(t,-1.5) &= \rho_2 \\ q_2(t,-1.5) &= \rho_2 q_1(t,0) \\ q_3(t,-1.5) &= 0 \\ q_4(t,-1.5) &= \frac{p_2}{\kappa-1} + \frac{1}{2}\frac{q_2(t,0)^2}{u_1(t,0)} \end{aligned}$$

at the left boundary (supersonic inflow) and

$$\begin{aligned} q_2(t,1.5) &= 0 \\ q_1(t,1.5) &= \rho_1, \quad \text{if } u(t,1.5) < 0, \end{aligned}$$

at the right boundary (one or two incoming characteristics).

6.4. Numerical Solution

The shock detector parameter is chosen as $\alpha_s = 100$ and the buffer stencil width is $N_{\text{sep}} = 4$. In all cases CFL = 0.5 is used and the time step is estimated by

$$\tau = \text{CFL}\left[\max_{\mathscr{D}}\left(\frac{u}{h_x}, \frac{u-c_s}{h_x}, \frac{u+c_s}{h_x}\right) + \max_{\mathscr{D}}\left(\frac{v}{h_y}, \frac{v-c_s}{h_y}, \frac{v+c_s}{h_y}\right)\right]^{-1}.$$

In Figs. 14–17 we compare pressure $p = (\kappa-1)(E - \rho q/2)$ and vorticity $\omega = \partial_x v - \partial_y u$ distributions for $N_x = 60$, $N_y = 40$ and $N_x = 120$, $N_y = 80$, respectively, obtained

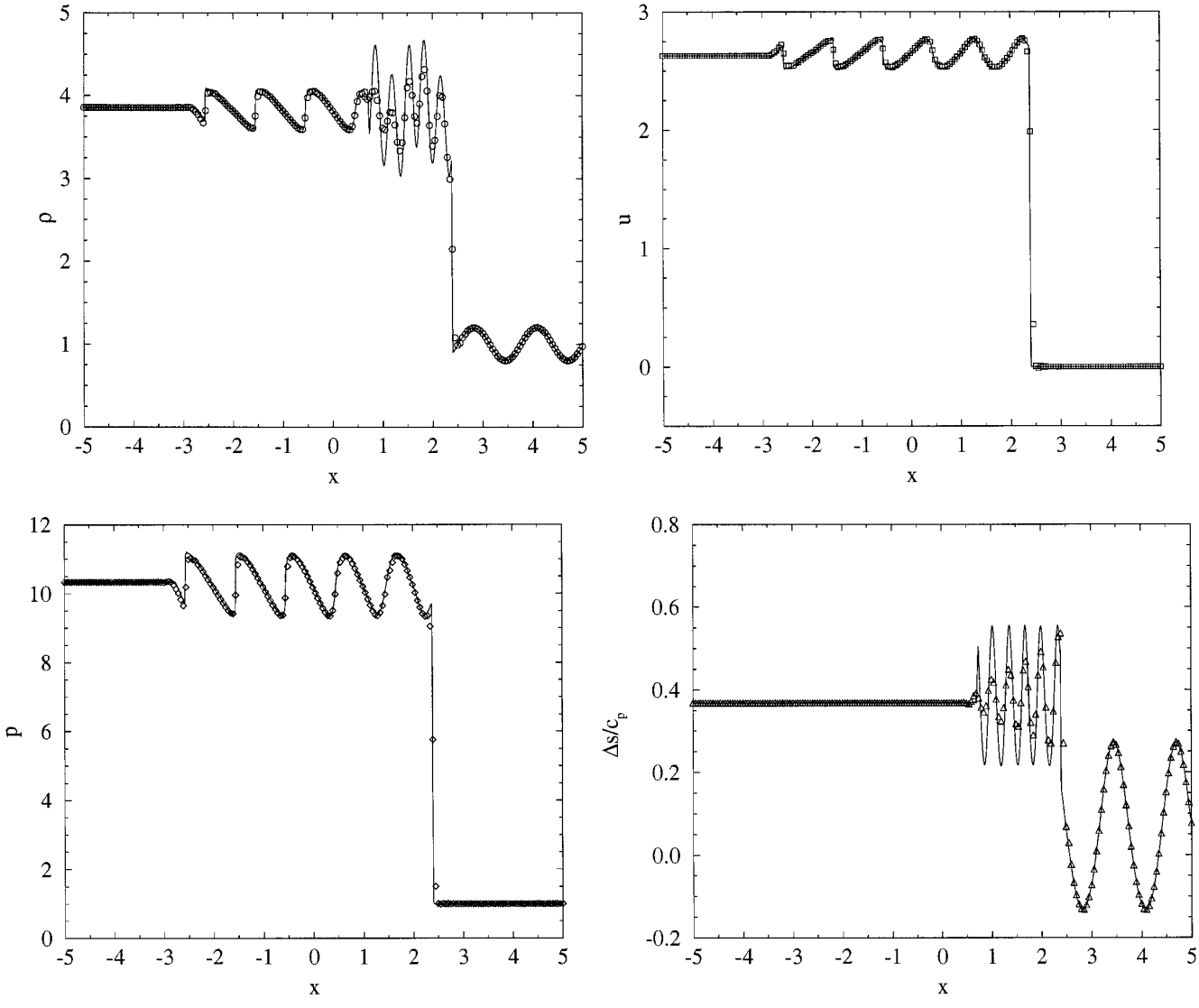

FIG. 12. Same as Fig. 11, except $N = 200$.

with the hybrid scheme CUHDE5R3, with results obtained with a pure Roe-flux ENO scheme, in our terminology, E4TVDR3.

For the hybrid scheme with the discretization $N_x = 120$, $N_y = 80$ an average of 10.9% of the grid points in x within one cluster were treated with the ENO procedure while in y the ENO scheme was inactive.

For a comparison with linear theory [28] we increase the streamwise domain to $-1.5 \le x \le 3.5$ and the integration time to $t = 0.4$. The amplitude of the incident vorticity waves is reduced to 10% so that the linearized theory is valid. The amplification rate of the incident vorticity wave across the shock is then obtained similarly as in [42] by averaging the Fourier coefficient of the second term of the solutions' Fourier expansion in y between the upstream wavefront and the shock at $t = 0.4$. Table V shows the relative errors between linear theory and computation for three different schemes and different grid spacing; the resolution in y is fixed at $N_y = 20$.

7. CONCLUSION

From recent work on direct numerical simulations of transitional flow using high-order compact finite-difference schemes [2, 30, 31, 36] it appears to be desirable to suppress poorly resolved waves by some numerical dissipation restricted to these waves. In [31] this is done by using an explicit filter function [26] at some time

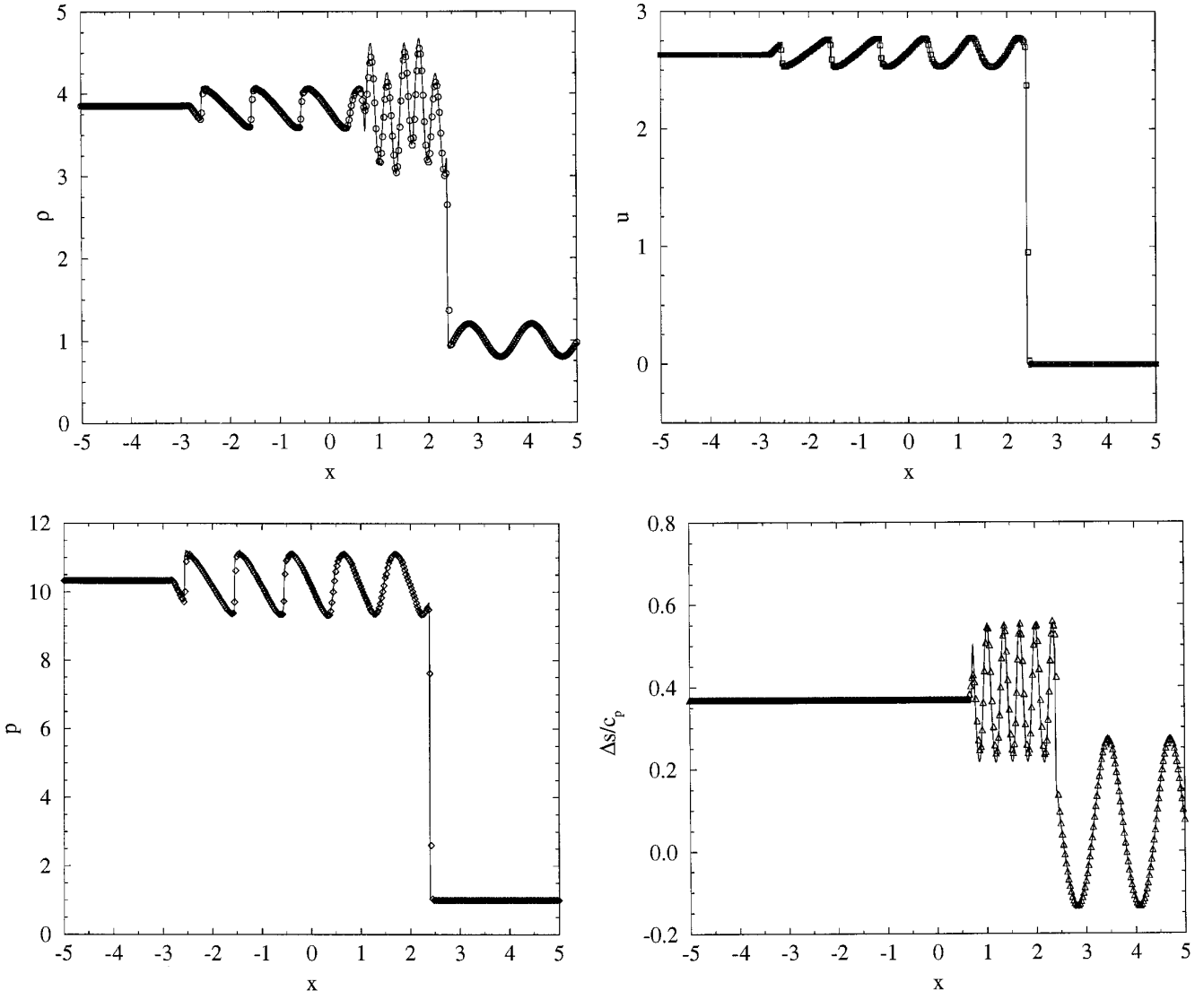

FIG. 13. Same as Fig. 11, except $N = 400$.

steps. From the most general formulation of a finite-difference scheme, high-order, upwind biased, centered compact schemes can be derived which preserve the good dispersion relation representation for resolved wave numbers while suppressing non-resolved ones due to their implicit dissipation. The compact stencil also allows one to find stable boundary closures of consistently high order. Weak solutions can be represented if discontinuities are treated by an ENO scheme. The coupling region between the compact upwind scheme and the ENO scheme functions as a source of spurious waves. Numerical experiments show that the less dissipative scheme CULD is more prone than the more dissipative scheme CUHD to exhibit spurious oscillations emanating into the smooth regions of the solution. The scheme resulting from a hybridization of a sufficiently dissipative compact upwind scheme and a high order ENO scheme combines the advantages of the compact schemes in smooth regions with a sharp representation of discontinuities and correct discontinuity convection.

TABLE V

Relative Errors of Amplification Rates

h	E4TVDR3	CUHDE5R3	CULDE5R3
0.02	−36.27%	−20.19%	−16.87%
0.01	−12.38%	−11.52%	−9.71%
0.007	−9.14%	−6.70%	−8.20%

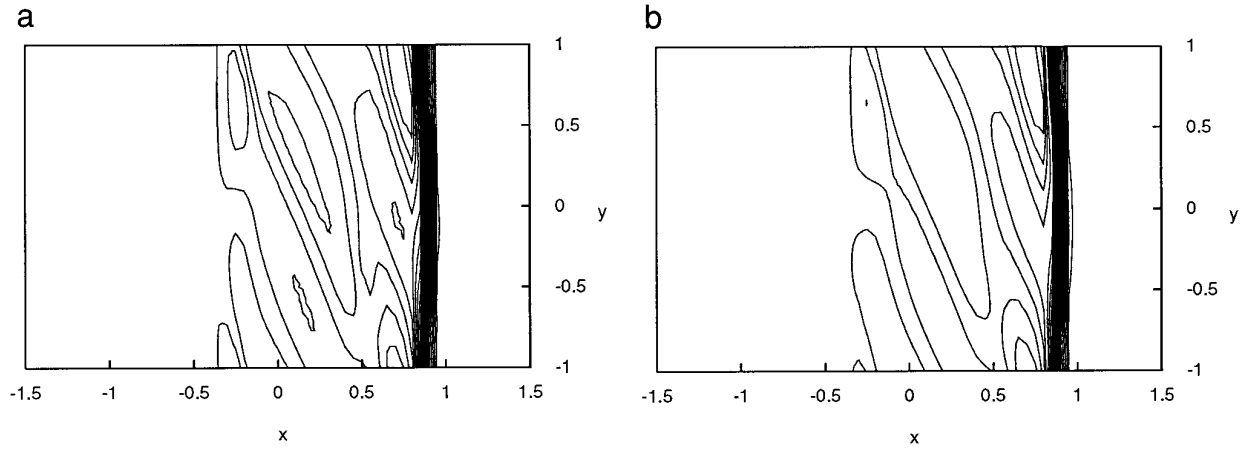

FIG. 14. Pressure p, $N_x = 60$, $N_y = 40$; 29 contours between min and max; (a) CUHDE5R3, $0.99 \le p \le 80.29$; (b) E4TVDR3, $0.99 \le p \le 80.12$.

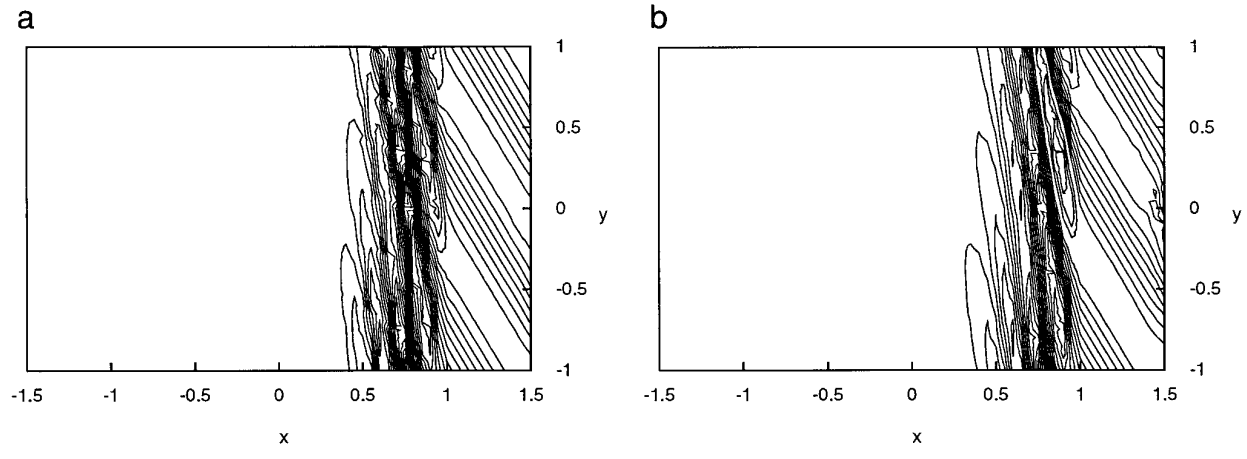

FIG. 15. Vorticity ω, $N_x = 60$, $N_y = 40$; 15 contours between min and max; (a) CUHDE5R3, $-14.67 \le \omega \le 15.03$; (b) E4TVDR3, $-14.32 \le \omega \le 14.82$.

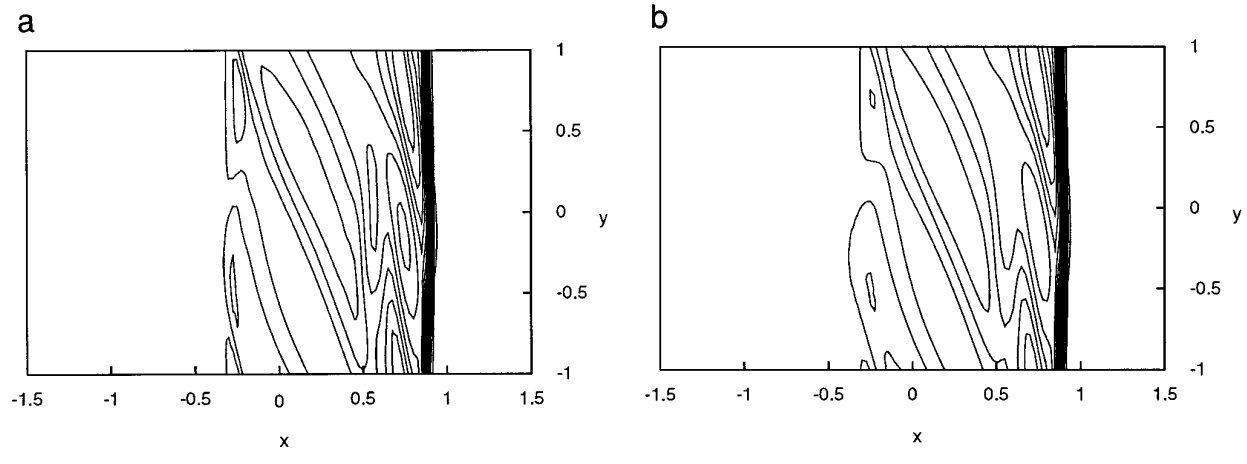

FIG. 16. Pressure p, $N_x = 120$, $N_y = 80$; 29 contours between min and max; (a) CUHDE5R3, $1.00 \le p \le 80.42$; (b) E4TVDR3, $0.99 \le p \le 80.45$.

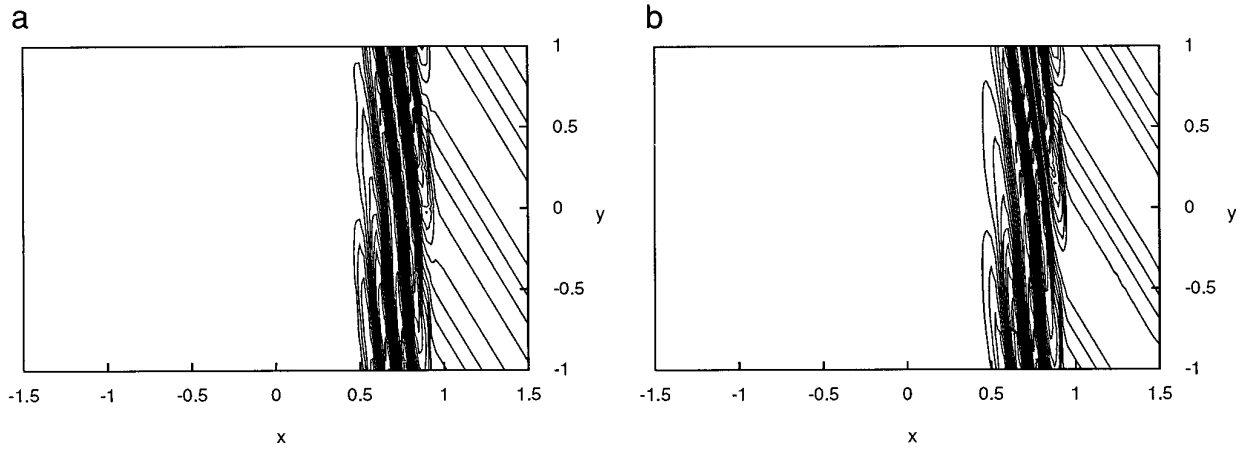

FIG. 17. Vorticity ω, $N_x = 120$, $N_y = 80$; 15 contours between min and max; (a) CUHDE5R3, $-34.02 \le \omega \le 32.47$; (b) E4TVDR3, $-28.92 \le \omega \le 27.96$.

APPENDIX A: COEFFICIENTS FOR SCHEMES CUHD AND CULD

In this appendix we give the coefficients for the proposed upwind scheme (positively biased) calculated with 14 digit precision, Tables VI and VII. The data may also be obtained in soft form by anonymous ftp from rft30.nas.nasa.gov. The components of the corresponding negatively biased upwind scheme can be obtained by multiplying $\mathbf{M}_L$ by $\mathbf{P}$ and $\mathbf{M}_R$ by $-\mathbf{P}$, where $\mathbf{P} = \lfloor 1 \cdots 1 \rceil$ is the reverse unit matrix.

APPENDIX B. EXAMPLE FOR A NON-UNIFORM GRID

We consider the model-advection equation (11). A mapping $[-1, 1] \to [-1, 1]$ which satisfies the assumptions of Section 2.3 for small enough δ is given by $x(\eta) = \delta\eta^2 + \eta$. For a non-compact centered scheme (three point stencil) we have

$$\alpha_{-1} = 0, \alpha_0 = 1, \alpha_1 = 0; \quad \alpha_{-1} = -1/2, a_0 = 0, a_1 = 1/2.$$

Using relations given in Section 2.3 we get readily for the exact dispersion relation

$$\tilde{\omega}(\xi; x) = ce^{-i\xi\delta}\sin(\xi).$$

Equation (29), with $\chi_1 = \chi_{-1} = \delta$ and $\chi_0 = 0$, yields $\varepsilon = \delta$ and for the first-order approximation in Eq. (28):

$$\tilde{\omega}(\xi; x) \doteq (1 - \mathbf{i}\xi\delta)\tilde{\omega}(\xi; \eta).$$

TABLE VI

Coefficients for Scheme CUHD

	$\alpha_{\mu_l}, \ldots, \alpha_{\mu_r}$				
ZS	0.035849272999368	0.7337612221857	1.	−0.1690430965563	−0.061336408258671
LB1	1.	−3.060761248017	−9.282568787503	—	—
LB2	−0.2230932216534	1.	2.651474320602	−0.1247233395454	—
RB2	15.74839515424	27.04931646417	1.	−0.3211206221354	—
RB1	4.850969558221	7.826957363797	1.	—	—
	$a_{\nu_l}, \ldots, a_{\nu_r}$				
ZS	−0.1760401349801	−1.137476930424	1.062649434339	0.4520614721441	−0.201193841079
LB1	−2.091690420288	12.73901356502	−7.591141872026	−3.324665234327	0.2684839616238
LB2	0.4461273501236	−3.555717436788	2.356364674278	0.8662558019092	−0.1130303895232
RB2	−1.846602572079	−30.2283794418	21.15923086495	12.27649588754	−1.36074473861
RB1	0.0020010162019952	−0.6538343569155	−8.740436045696	5.756444175312	3.635825211098

Note. Abbreviations are the same as Table I.

TABLE VII

Coefficients for Scheme CULD

	$\alpha_{\mu_l}, \ldots, \alpha_{\mu_r}$				
ZS	0.027844800835984	0.455868829489	1.	0.4774791908094	0.038825537571968
LB1	1.	−3.060761248017	−9.282568787503	—	—
LB2	−1.384173201496	1.	6.620636755258	−2.122934969145	—
RB2	15.74839515424	27.04931646417	1.	−0.3211206221354	—
RB1	4.074311507054	6.58361830343	1.	—	—
	$a_{\nu_l}, \ldots, a_{\nu_r}$				
ZS	−0.118727423955	−0.7482059425882	0.00052666822731662	0.7184558284235	0.1479508698924
LB1	−2.091690420288	12.73901356502	−7.591141872026	−3.324665234327	0.2684839616238
LB2	3.362325146817	−11.84525146073	8.836922058206	0.2990810938894	−0.6530768381839
RB2	−1.846602572079	−30.2283794418	21.15923086495	12.27649588754	−1.36074473861
RB1	0.040891100302009	−0.7577318529877	−6.875427455145	4.202556257561	3.38971195027

Note. Abbreviations are the same as Table I.

The latter expression is obviously equivalent to the first-order approximation of $\varpi(\xi; x)$ in terms of δ.

ACKNOWLEDGMENTS

The authors are grateful to Dr. H. C. Yee, NASA Ames Research Center, and Professor R. D. Moser, University of Illinois, for their valuable comments on a draft of this paper. The first author also wants to remark that the idea of extending the formulation of symmetric compact schemes to upwind biased schemes as presented herein originates from several discussions with Dr. Neil Sandham, Queen Mary and Westfield College, London.

REFERENCES

1. N. A. Adams, ''Numerical Study of Boundary Layer Interaction with Shocks—Method and Code Validation,'' in *CTR Annual Research Briefs 1994*, Center for Turbulence Research, Stanford University and NASA Ames Research Center, Stanford, CA, 1994.
2. N. A. Adams and L. Kleiser, *J. Fluid Mech.*, to appear.
3. M. H. Carpenter, D. Gottlieb, and S. Abarbanel, *J. Comput. Phys.* **108,** 272 (1993).
4. B. Cockburn and C.-W. Shu, *SIAM J. Numer. Anal.* **31,** 607 (1994).
5. L. Collatz, *Numerische Behandlung von Differentialgleichungen* (Springer-Verlag, Berlin, 1955).
6. F. Dexun, M. Yanwen, and L. Hong, ''Upwind Compact Schemes and Applications,'' in *Proceedings, 5th Symp. on Comput. Fluid Dyn.,* Vol. 1, Japan Soc. of Comput. Fluid Dyn., 1993.
7. D. Gottlieb and S. A. Orszag, *Numerical Analysis of Spectral Methods: Theory and Applications* (SIAM-CBMS, Philadelphia, 1986).
8. Y. Guo and N. A. Adams, ''Numerical Investigation of Supersonic Turbulent Boundary Layers with High Wall Termperature,'' in *CTR Proceedings of the 1994 Summer Program, Center for Turbulence Research, Stanford University and NASA Ames Research Center* (Stanford, CA, 1994).
9. B. Gustafsson, *Math. Comput.* **29,** 396 (1975).
10. B. Gustafsson, H.-O. Kreiss, and J. Oliger, *Time Dependent Problems and Difference Methods* (Wiley, New York, 1995).
11. B. Gustafsson, H.-O. Kreiss, and A. Sundström, *Math. Comput.* **26,** 649 (1972).
12. E. Hairer, S. P. Nørsett, and G. Wanner, *Solving Ordinary Differential Equations. Vol. I. Nonstiff Problems* (Springer Verlag, Berlin, 1987).
13. Z. Haras and S. Ta'asan, *J. Comput. Phys.* **114,** 265 (1994).
14. A. Harten, *J. Comput. Phys.* **49,** 357 (1983).
15. A. Harten and S. R. Chakravarthy, Technical Report 91–76, ICASE, NASA Langley Research Center, Hampton, Virginia, 1991; CAM Report 91–16, UCLA, Los Angeles (unpublished).
16. A. Harten, B. Engquist, S. Osher, and S. R. Chakravarthy, *J. Comput. Phys.* **71,** 231 (1987).
17. A. Harten, P. D. Lax, and B. van Leer, *SIAM Rev.* **25**(1), 35 (1983).
18. A. Harten and G. Zwas, *J. Comput. Phys.* **9,** 568 (1972).
19. R. S. Hirsh, *J. Comput. Phys.* **19,** 90 (1975).
20. T. Y. Hou and P. G. Le Floch, *Math. Comput.* **62,** 497 (1994).
21. Z. Kopal, *Numerical Analysis* (Springer-Verlag, New York, 1966).
22. H.-O. Kreiss and J. Lorenz, *Initial-Boundary Value Problems and the Navier–Stokes Equations* (Academic Press, London, 1989).
23. H.-O. Kreiss, S. A. Orszag, and M. Israeli, *Annu. Rev. Fluid Mech.* **6,** 281 (1974).
24. H.-O. Kreiss and L. Wu, *Appl. Numer. Math.* **12,** 213 (1993).
25. F. Lafon and S. Osher, *J. Comput. Phys.* **96,** 110 (1991).
26. S. K. Lele, *J. Comput. Phys.* **103,** 16 (1992).
27. D.-K. Mao, *J. Comput. Phys.* **92,** 422 (1991).
28. J. F. McKenzie and K. O. Westphal, *Phys. Fluids* **11,** 2350 (1968).
29. C. D. Pruett and C.-L. Chang, *Theor. Comput. Fluid Dyn.,* **7,** 397 (1995).
30. C. D. Pruett and T. Zang, *Theor. Comput. Fluid Dyn.* **3,** 345 (1992).
31. C. D. Pruett, T. Zang, C.-L. Chang, and M. H. Carpenter, *Theor. Comput. Fluid Dyn.* **7,** 49 (1995).
32. M. M. Rai and P. Moin, *J. Comput. Phys.* **93,** 169 (1993).
33. S. C. Reddy and L. N. Trefethen, *Numer. Math.* **62,** 235 (1992).
34. P. L. Roe, *Annu. Rev. Fluid Mech.* **18,** 337 (1986).
35. A. M. Rogerson and E. Meiburg, *J. Sci. Comput.* **5**(2), 151 (1990).
36. N. D. Sandham and W. C. Reynolds, *J. Fluid Mech.* **224,** 133 (1991).

37. K. Schittkowski, *Annu. Oper. Res.* **5,** 485 (1985).
38. C.-W. Shu, *SIAM J. Sci. Stat. Comput.* **9**(6), 1073 (1988).
39. C.-W. Shu, *J. Sci. Comput.* **5**(2), 127 (1990).
40. C.-W. Shu and S. Osher, *J. Comput. Phys.* **77,** 439 (1988).
41. C.-W. Shu and S. Osher, *J. Comput. Phys.* **83,** 32 (1989).
42. C.-W. Shu, T. A. Zang, G. Erlebacher, D. Whitaker, and S. Osher, *Appl. Numer. Math.* **9,** 45 (1992).
43. J Stoer, ''Principles of Sequential Quadratic Programming Methods for Solving Nonlinear Problems, in *Computational Mathematical Programming*, edited by K. Schittkowski, NATO ASI Series F, Vol. 15, (Springer-Verlag, Berlin, 1985), p. 165.
44. J. C. Strikwerda, *Finite Difference Schemes and Partial Differential Equations* (Wadsworth & Brooks/Cole, Belmont, CA, 1989).
45. P. A. Thompson, *Compressible-Fluid Dynamics*, Advanced Engineering Series. (Rensselaer Polytechnic Institute, Troy, NY, 1988).
46. A. I. Tolstykh, ''High Accuracy Methods for Compressible Navier–Stokes Equations,'' in *Proceedings, 5th Int. Symp. on Comput. Fluid Dyn.,* Vol. 3, Japan Soc. of Comput. Fluid Dyn., 1993.
47. L. N. Trefethen, *SIAM Rev.* **24,** 113 (1982).
48. J. H. Williamson, *J. Comput. Phys.* **35,** 48 (1980).
49. S. Wolfram, *Mathematica. A System for Doing Mathematics by Computer*, 2nd ed., (Addison–Wesley, Redwood City, CA, 1991).
50. H. C. Yee, Technical Report TM-101088, NASA, NASA Ames Research Center, Moffet Field, CA 94035, 1989; Von Kármán Institute, Lecture Series 1989–04 (unpublished).